MATCH
Communications in Mathematical and in Computer Chemistry

MATCH Commun. Math. Comput. Chem. **97** (2027) 1057–1105
ISSN: 0340–6253
doi: 10.46793/match.97-3.27226

A Saturated Autocatalytic Model with Phenomenological Thermal Activation: Continuous Dynamics, Diffusion-Driven Patterns, and Discretization Effects

Saad Jamhan Aldosari[a], Muhammad Sajjad Shabbir[b,*], Asifa Tassaddiq[c], Salah Knani[d], Rizwan Ahmed[e]

[a] *Department of Mathematics, College of Science and Humanities in Alkharj, Prince Sattam Bin Abdulaziz University, Alkharj 11942, Saudi Arabia*

[b] *Department of Mathematics, University of Poonch Rawalakot, Rawalakot 12350, Azad Jammu and Kashmir, Pakistan*

[c] *Department of Information Technology, College of Computer and Information Sciences, Majmaah University, Al Majmaah 11952, Saudi Arabia*

[d] *Center for Scientific Research and Entrepreneurship, Northern Border University, Arar 73213, Saudi Arabia*

[e] *International Center for Interdisciplinary Research in Sciences, The University of Lahore, Lahore, Pakistan*

sajjadmust@gmail.com

(Received July 20, 2026)

Abstract

We formulate a two-intermediate model for precursor-fed autocatalysis with a bounded phenomenological thermokinetic factor. Positivity, dissipativity, existence of a positive equilibrium, an a

*Corresponding author.

priori equilibrium bound, and a conditional uniqueness criterion are established analytically. Generic saddle-node and Hopf conditions are stated with their nondegeneracy hypotheses. Numerical continuation identifies two transversal Hopf points with negative first Lyapunov coefficients under a specified eigenvector normalization. For the reaction–diffusion extension, global positivity and boundedness are established, and an exact finite-domain instability test is obtained by coupling the kinetic Jacobian to the Neumann spectrum. Fully specified grayscale simulations produce noise-selected spots and mode-selected stripe and square-symmetric structures. A positive semi-implicit discretization is then examined as a numerical dynamical system. The scheme preserves non-negative concentrations and equilibria, but the reference fixed point loses Schur stability at $h_c \approx 0.617496$, whereas the exact sampled flow remains stable. Step refinement further shows that $h < h_c$ is not an accuracy condition. Coarse-step periodic and positive-exponent responses are therefore attributed to the numerical map rather than to the planar chemical flow. The analysis separates chemical admissibility, homogeneous stability, spatial-mode stability, numerical fixed-point stability, and trajectory accuracy.

1 Introduction

Autocatalytic and thermokinetic reaction systems are standard models for nonlinear chemical dynamics. Compact kinetic mechanisms can produce induction, overshoot, damped oscillations, sustained oscillations, and multiple stationary states because production feedback competes with removal and heat loss. A useful reduced model must therefore preserve nonnegative concentrations, control high-concentration growth, and identify the parameter combinations at which stationary states lose stability.

The Belousov–Zhabotinsky reaction and the Oregonator are classical examples of reduced oscillatory chemistry [15, 37]. The Brusselator, Sel'kov, and Gray–Scott families likewise show how low-dimensional source–feedback–loss structures generate stationary and periodic responses [17, 18, 28, 34]. General accounts of chemical oscillation and thermokinetic feedback are available in [14, 28, 33], while recent reduced models continue to examine oscillatory response, thermokinetic tipping, and higher-codimension bifurcation structure [10, 13, 16, 24, 32].

The kinetic construction is motivated by the cubic autocatalytic mecha-

nism studied by Merkin, Needham and Scott [25], but the constant precursor-pool approximation used here represents sustained or slowly varying supply rather than a closed vessel. The route $A + 2B \to 3B$ provides positive feedback: one molecule of A is consumed and one net molecule of the autocatalyst B is produced. A background route $A \to B$ seeds the loop. The present model adds saturation, cross-quenching $A + B \to E$, bimolecular termination $2B \to D$, and a bounded concentration-dependent activation factor. The latter is stated explicitly as a phenomenological thermal closure rather than as an exact elimination of an energy equation.

Positive finite-difference schemes are attractive for chemical kinetics because negative concentrations are inadmissible, but positivity alone does not preserve fixed-point type, stability, invariant sets, or trajectory accuracy. Topological and elementary dynamic consistency provide stronger criteria [2, 8]. Stability changes under positive discretization have been analysed for two-dimensional systems, including the Sel'kov and Lengyel–Epstein models [29]. Related studies combine Hopf analysis with consistency-preserving discretizations of autocatalytic systems, while recent work examines strong resonances and two-parameter bifurcations in a discrete glycolysis model [11, 12, 22]. Other dynamically consistent constructions suppress step-dependent spurious bifurcations [3, 9, 26, 27]. In contrast to studies that regard the discrete system as the primary model, the map considered here is assessed solely as an approximation of the continuous flow.

This distinction is essential because the continuous model is planar and autonomous. In a compact invariant region it may possess equilibria and limit cycles, but not deterministic chaos, by the Poincaré–Bendixson theorem [19, 35]. Positive-exponent or high-period behaviour generated by a coarse numerical step must therefore be compared with exact-flow multipliers and step-refinement results before any chemical interpretation is considered.

Spatial transport poses a distinct stability problem. Diffusion can destabilize an asymptotically stable homogeneous state and select an intrinsic spatial scale through the mechanism introduced by Turing [36]. Stationary structures have been observed in open chemical media [4, 30].

Recent reaction–diffusion studies address equilibrium patterns, spatiotemporal oscillations, instability of periodic solutions, and topology-dependent pattern selection in enzyme-catalysed and related chemical systems [5–7, 38, 39]. Numerical methods that preserve positivity have also been developed for autocatalytic glycolysis reaction–diffusion equations [21]. These contributions establish the broader methodology. The present analysis instead focuses on a bounded saturated rate law, the actual finite-domain Neumann spectrum, qualified numerical convergence of stationary patterns, and the distinction between spatial instability and discretization-induced dynamics. Experimental Turing patterns motivate the analysis but do not validate the phenomenological kinetics.

The results are specific to the proposed rate law. Its bounded form permits direct proofs of positivity, dissipativity, equilibrium existence, and a finite equilibrium bound. The scalar equilibrium reduction links saddle-node degeneracy to the determinant of the full kinetic Jacobian, while normal-form calculations determine the criticality of two Hopf points. The reaction–diffusion extension yields an exact finite-domain Neumann-mode test and conditional nonlinear pattern simulations. Finally, a positive semi-implicit update provides a controlled example in which chemical admissibility is preserved but fixed-point stability and trajectory accuracy are lost as the step increases. Standard Turing and discrete-bifurcation criteria are used as established tools and are not presented as general methodological innovations.

2 Basic precursor-fed cubic autocatalytic model

The basic reaction skeleton consists of a precursor, two dynamic intermediates, and an inert product:

$$P \xrightarrow{k_0} A, \qquad A + 2B \xrightarrow{k_c} 3B, \qquad B \xrightarrow{k_b} C. \tag{1}$$

The chemical species A is produced from the precursor P. It is not itself the autocatalyst. The autocatalytic species is B, because two molecules of

B participate in the conversion of one molecule of A into three molecules of B. The net effect of the second step is the consumption of one molecule of A and the production of one additional molecule of B. The final step removes B from the active reaction pool.

Let

$$a(t) = [A], \qquad b(t) = [B] \tag{2}$$

be concentrations. In a pool approximation, the precursor concentration is represented by an effective constant p_0 over the main response interval. Under mass-action kinetics the three rates are

$$r_0 = k_0 p_0, \qquad r_c = k_c a b^2, \qquad r_b = k_b b. \tag{3}$$

The resulting two-variable model is

$$\frac{da}{dt} = k_0 p_0 - k_c a b^2, \qquad \frac{db}{dt} = k_c a b^2 - k_b b. \tag{4}$$

Thus the reaction skeleton (1) leads to the base mass-action system (4). This model is useful for identifying the source-feedback-loss balance, but it is chemically restrictive. It assumes unbounded cubic efficiency at high B, no non-catalytic conversion from A to B, no cross-removal of intermediates, no radical termination, and no thermal feedback. Each of these simplifications can affect the qualitative response.

A first chemical correction is the background route

$$A \xrightarrow{k_u} B. \tag{5}$$

The route (5) supplies B even when the cubic term is weak because b is small. It can represent slow thermal conversion, spontaneous decomposition, photochemical activation, or a weak redox route. It is especially important in precursor-pool dynamics, where the onset of autocatalysis may be delayed unless some seed concentration of the autocatalyst is produced.

3 Saturated autocatalytic mechanism with thermal activation

The proposed reaction network is

$$P \xrightarrow{k_0} A, \qquad A \xrightarrow{k_u} B, \qquad A + 2B \longrightarrow 3B, \tag{6}$$

$$B \xrightarrow{k_b} C, \qquad A + B \xrightarrow{k_s} E, \qquad 2B \xrightarrow{k_q} D. \tag{7}$$

Equations (6)–(7) display the source, background conversion, autocatalysis, decay, cross-quenching, and termination routes used in the reduced mechanism. The effective rate of the autocatalytic step is not written as a constant multiple of ab^2. Instead, it is taken as

$$r_c = \frac{k_c a b^2}{1 + \sigma b^2} \Phi(b), \qquad \Phi(b) = \exp\left(\frac{\eta b}{K_T + b}\right). \tag{8}$$

Figure 1 summarizes the reaction architecture.

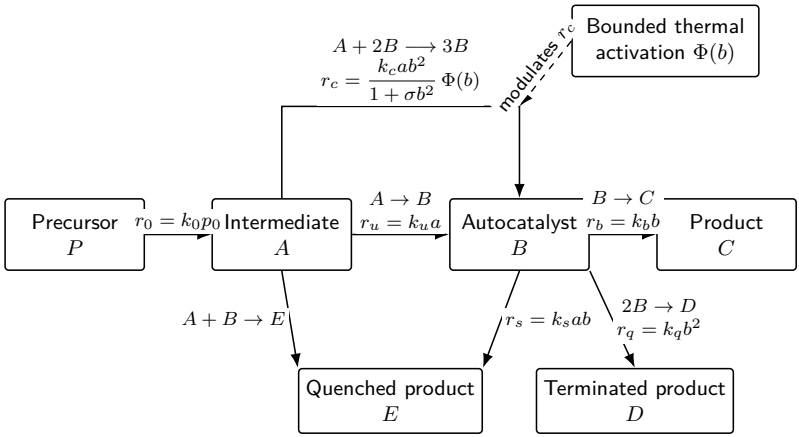

Figure 1. Reduced reaction architecture. The active variables are the intermediate concentrations $a(t) = [A]$ and $b(t) = [B]$. Solid arrows denote material-conversion routes, and the dashed arrow denotes phenomenological thermal modulation of the autocatalytic rate. The two arrows entering E indicate the joint consumption of A and B by cross-quenching.

The denominator $1 + \sigma b^2$ represents saturation of the cubic autocat-

alytic route. It can be interpreted as finite encounter efficiency, crowding of a reactive intermediate, limited active sites, solvent-cage inhibition, or diffusion limitation. The parameter σ is not a new reaction by itself; it is an effective coefficient that reduces the productivity of the autocatalytic channel when B becomes large.

The multiplier $\Phi(b)$ is a reduced thermokinetic factor. It increases with b under the assumption that formation of the active intermediate is associated with heat-assisted conversion, and it remains bounded to represent finite thermal activation. Temperature is not an independent state variable; consequently, Φ is a phenomenological concentration-dependent closure rather than a thermodynamically complete energy model.

3.1 Reduced thermal activation assumption

A full thermokinetic mechanism would augment the concentration equations by an energy balance, for example

$$C_h \frac{dT}{dt} = q_h r_c - H(T - T_0), \tag{9}$$

where T_0 is the bath temperature, C_h is an effective heat capacity, q_h is the heat released per unit conversion, and H is a heat-transfer coefficient. A quasi-steady reduction of (9) would relate $T - T_0$ to the heat-generating reaction rate. Here, b is instead used as a bounded proxy for thermal activation:

$$T - T_0 \approx \Theta_{\max} \frac{b}{K_T + b}. \tag{10}$$

Equation (10) is a phenomenological closure, not an exact consequence of (9). It states only that larger amounts of the active intermediate are associated with stronger heat-assisted conversion and that finite heat removal limits the effective temperature rise. The assumption should be tested against an explicit temperature equation when a specific reaction and calorimetric data are available.

For an Arrhenius factor $\exp[-E/(RT)]$, expansion about T_0 gives

$$\exp\left[-\frac{E}{RT}\right] = \exp\left[-\frac{E}{RT_0}\right] \exp\left(\frac{E}{RT_0^2}(T - T_0) + O((T - T_0)^2)\right). \tag{11}$$

After absorbing the constant prefactor into k_c and substituting (10), the reduced multiplier becomes

$$\Phi(b) = \exp\left(\frac{\eta b}{K_T + b}\right), \qquad \eta = \frac{E\Theta_{\max}}{RT_0^2}. \tag{12}$$

When $\eta = 0$, the model is isothermal. The parameter K_T specifies the concentration scale over which the effective thermal contribution approaches saturation.

3.2 Dimensional kinetic equations

The full dimensional rates are

$$r_0 = k_0 p_0, \quad r_u = k_u a, \quad r_c = \frac{k_c a b^2}{1 + \sigma b^2} \exp\left(\frac{\eta b}{K_T + b}\right), \quad r_b = k_b b, \tag{13}$$

$$r_s = k_s a b, \qquad r_q = k_q b^2. \tag{14}$$

Hence the dimensional model is

$$\frac{da}{dt} = k_0 p_0 - k_u a - \frac{k_c a b^2}{1 + \sigma b^2} \exp\left(\frac{\eta b}{K_T + b}\right) - k_s a b, \tag{15}$$

$$\frac{db}{dt} = k_u a + \frac{k_c a b^2}{1 + \sigma b^2} \exp\left(\frac{\eta b}{K_T + b}\right) - k_b b - k_s a b - 2k_q b^2. \tag{16}$$

The factor 2 in front of $k_q b^2$ in (16) follows from the stoichiometry $2B \to D$: two molecules of B are lost per termination event. The dimensional parameters and their chemical interpretations are summarized in Table 1.

4 Non-dimensionalization

Let $C_* > 0$ be a reference concentration and let

$$x = \frac{a}{C_*}, \qquad y = \frac{b}{C_*}, \qquad \tau = k_b t. \tag{17}$$

Table 1. Dimensional parameters and chemical interpretations.

Symbol	Meaning	Chemical role
p_0	effective precursor level	reservoir or slowly varying supply of A
k_0	precursor activation constant	rate of $P \to A$ production
k_u	background conversion constant	non-catalysed $A \to B$ route
k_c	autocatalytic constant	strength of $A + 2B \to 3B$
σ	saturation coefficient	finite efficiency of cubic conversion
η	thermal activation strength	intensity of reduced heat feedback
K_T	thermal saturation level	concentration scale for heat activation
k_b	first-order decay constant	removal of B to C
k_s	cross-quenching constant	removal by $A + B \to E$
k_q	termination constant	nonlinear loss by $2B \to D$

Define positive dimensionless parameters by

$$\alpha = \frac{k_0 p_0}{k_b C_*}, \qquad \beta = \frac{k_u}{k_b}, \qquad \gamma = \frac{k_c C_*^2}{k_b}, \qquad s = \sigma C_*^2, \tag{18}$$

$$\rho = \frac{k_s C_*}{k_b}, \qquad \delta = \frac{2k_q C_*}{k_b}, \qquad \lambda = \eta, \qquad \kappa = \frac{K_T}{C_*}. \tag{19}$$

Then (15)–(16) reduce to

$$\frac{dx}{d\tau} = f(x, y) = \alpha - \beta x - \mathcal{R}(y)x - \rho xy, \tag{20}$$

$$\frac{dy}{d\tau} = g(x, y) = \beta x + \mathcal{R}(y)x - y - \rho xy - \delta y^2, \tag{21}$$

where

$$\mathcal{R}(y) = \frac{\gamma y^2}{1 + sy^2} \exp\left(\frac{\lambda y}{\kappa + y}\right), \qquad y \geq 0. \tag{22}$$

The effective rate function (22) is the dimensionless saturated autocatalytic rate with phenomenological thermal activation. For later Hopf calculations, it is useful to record the higher derivatives of $\mathcal{R}$. For $y > 0$, write $\mathcal{R}'(y) = \mathcal{R}(y)L_1(y)$, where

$$L_1(y) = \frac{2}{y} - \frac{2sy}{1+sy^2} + \frac{\lambda\kappa}{(\kappa+y)^2}. \tag{23}$$

Then

$$\begin{aligned} \mathcal{R}''(y) &= \mathcal{R}(y)\{L_1(y)^2 + L_2(y)\}, \\ \mathcal{R}'''(y) &= \mathcal{R}(y)\{L_1(y)^3 + 3L_1(y)L_2(y) + L_3(y)\}. \end{aligned} \tag{24}$$

with

$$L_2(y) = -\frac{2}{y^2} - \frac{2s(1-sy^2)}{(1+sy^2)^2} - \frac{2\lambda\kappa}{(\kappa+y)^3}, \tag{25}$$

$$L_3(y) = \frac{4}{y^3} + \frac{4s^2y(3-sy^2)}{(1+sy^2)^3} + \frac{6\lambda\kappa}{(\kappa+y)^4}. \tag{26}$$

These expressions make the normal-form calculation in the Hopf section reproducible from the displayed rate law. All parameters in (18)–(19) are assumed to be strictly positive unless stated otherwise.

The dimensionless groups have the following roles. The parameter α is the precursor-feed strength. The parameter β measures direct $A \to B$ conversion relative to B decay. The parameter γ measures cubic autocatalytic strength. The parameter s controls saturation. The pair (λ, κ) controls effective thermal activation. The parameter ρ measures cross-quenching, and δ measures bimolecular termination of the autocatalyst.

4.1 Parameter selection and dimensional scale

The numerical parameter sets used below were selected by continuation and parameter screening to expose stable, Hopf, and coarse-step numerical regimes. They were not fitted to observations and are not estimates for a named reagent system. Taking $C_* = 10^{-3}\,\mathrm{mol\,L^{-1}}$ and $k_b = 0.1\,\mathrm{s^{-1}}$, the

reference values in (42) give

$$\begin{aligned} k_u &= 2.857 \times 10^{-2}\,\mathrm{s}^{-1}, \qquad k_c = 2.56739 \times 10^{6}\,\mathrm{L}^2\,\mathrm{mol}^{-2}\,\mathrm{s}^{-1}, \\ \sigma &= 1.5179 \times 10^{6}\,\mathrm{L}^2\,\mathrm{mol}^{-2}, \qquad k_s = 50.88\,\mathrm{L}\,\mathrm{mol}^{-1}\,\mathrm{s}^{-1}, \\ k_q &= 171.93\,\mathrm{L}\,\mathrm{mol}^{-1}\,\mathrm{s}^{-1}, \qquad K_T = 0.3591\,\mathrm{mmol}\,\mathrm{L}^{-1}, \end{aligned} \tag{27}$$

and $k_0 p_0 = 0.51523\,\mathrm{mmol}\,\mathrm{L}^{-1}\,\mathrm{s}^{-1}$. This dimensional reconstruction is illustrative and is not a parameter estimate for a specific reagent system. Quantitative prediction would require a specified mechanism, calorimetric measurements, and parameter estimation.

Figure 2 shows how the effective autocatalytic rate changes with λ and s. Increasing λ raises the rate curve because the thermal factor accelerates autocatalytic conversion. Increasing s suppresses the high-y part of the curve because saturation becomes stronger.

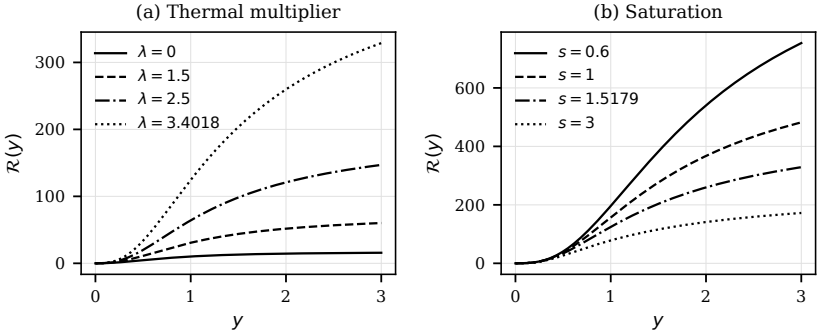

Figure 2. Effective autocatalytic rate $\mathcal{R}(y)$. Left: effect of the thermokinetic strength λ. Right: effect of the saturation coefficient s.

5 Positivity, dissipativity, and absorbing bounds

The first requirement for a chemical concentration model is invariance of the non-negative quadrant. The next result verifies this property.

Proposition 1 (Positive invariance)**.** *For positive parameters and initial*

data $(x(0), y(0)) \in \mathbb{R}^2_+$*, the solution of* (20)–(21) *remains in* $\mathbb{R}^2_+$ *for all times for which it exists.*

Proof. On the boundary $x = 0$, one has $f(0, y) = \alpha > 0$. Thus the vector field points into the non-negative quadrant. On the boundary $y = 0$, one has $g(x, 0) = \beta x \geq 0$. Hence the solution cannot cross into $y < 0$. The vector field is locally Lipschitz on $\mathbb{R}^2_+$. The standard boundary criterion for positive systems gives positive invariance. ■

Proposition 2 (Ultimate boundedness)**.** *Assume* $s > 0$ *and* $\delta > 0$*. Every non-negative solution of* (20)–(21) *is ultimately bounded.*

Proof. From (20),

$$\frac{dx}{d\tau} \leq \alpha - \beta x. \tag{28}$$

It follows that for every $\varepsilon > 0$ there is $T_1 > 0$ such that

$$x(\tau) \leq X_\varepsilon := \frac{\alpha}{\beta} + \varepsilon, \qquad \tau \geq T_1. \tag{29}$$

Since $s > 0$,

$$0 \leq \mathcal{R}(y) \leq \frac{\gamma}{s} \mathrm{e}^{\lambda} =: R_{\max}. \tag{30}$$

For $\tau \geq T_1$,

$$\frac{dy}{d\tau} \leq X_\varepsilon(\beta + R_{\max}) - \delta y^2. \tag{31}$$

Thus $y(\tau)$ is ultimately bounded above by any number larger than

$$Y_\varepsilon = \left(\frac{X_\varepsilon(\beta + R_{\max})}{\delta} \right)^{1/2}. \tag{32}$$

The two estimates give an absorbing rectangle in $\mathbb{R}^2_+$. Since the vector field is locally Lipschitz on $\mathbb{R}^2_+$, the absorbing estimate also excludes finite-time blow-up and extends every non-negative solution globally in time. ■

Remark. The condition $s > 0$ prevents indefinite growth of the effective cubic rate, while $\delta > 0$ gives a high-concentration termination mechanism for B. Both assumptions have direct chemical interpretations. If one of them is absent, boundedness may still hold for certain parameter ranges, but it is no longer guaranteed by the simple comparison argument above.

6 Equilibrium points

Set

$$Q(y) = \beta + \mathcal{R}(y), \qquad M(y) = Q(y) + \rho y. \tag{33}$$

At a positive equilibrium $E^* = (x^*, y^*)$, the equation $f(x^*, y^*) = 0$ gives

$$x^* = \frac{\alpha}{M(y^*)}. \tag{34}$$

Substitution into $g(x^*, y^*) = 0$ yields

$$\Psi(y) = \alpha Q(y) - yM(y) - \rho\alpha y - \delta y^2 M(y) = 0, \tag{35}$$

or equivalently

$$\Psi(y) = \alpha\{Q(y) - \rho y\} - M(y)y(1 + \delta y). \tag{36}$$

Thus the stationary problem reduces to a scalar root followed by (34). Figure 3 shows the reference function and a magnified view of its positive zero.

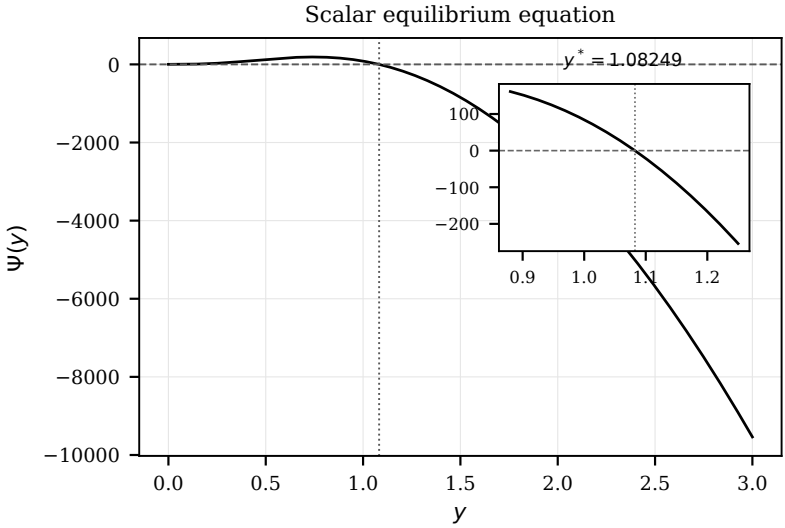

Figure 3. Scalar equilibrium function $\Psi(y)$ for the reference parameter set. The inset resolves the positive zero $y^* \approx 1.08249$.

Proposition 3 (Existence and an a priori equilibrium bound)**.** *For positive parameters with $s > 0$ and $\delta > 0$, system* (20)–(21) *has at least one positive equilibrium. Every positive equilibrium satisfies*

$$0 < y^* \le y_{\max} := \frac{-1 + \sqrt{1 + 4\delta\alpha}}{2\delta}. \tag{37}$$

Proof. At $y = 0$, (35) gives $\Psi(0) = \alpha\beta > 0$. Because $\mathcal{R}$ is bounded for $s > 0$, the negative term $-\delta y^2 M(y)$ forces $\Psi(y) \to -\infty$ as $y \to \infty$. Continuity therefore gives a positive zero, and (34) gives $x^* > 0$. Adding the two equilibrium equations yields

$$0 = \alpha - y^* - 2\rho x^* y^* - \delta (y^*)^2, \tag{38}$$

so $\delta(y^*)^2 + y^* \le \alpha$, which is equivalent to (37). ■

Proposition 4 (Conditional uniqueness)**.** *If*

$$\Psi'(y) < 0 \qquad \textit{for all } 0 < y \le y_{\max}, \tag{39}$$

then the positive equilibrium is unique.

Proof. Existence is already established and every positive zero lies in the compact interval (37). Condition (39) makes Ψ strictly decreasing on that interval, so it can vanish at most once. ■

Since

$$\mathcal{R}'(y) = \gamma \exp\left(\frac{\lambda y}{\kappa + y}\right)\left[\frac{2y}{(1+sy^2)^2} + \frac{y^2}{1+sy^2}\frac{\lambda\kappa}{(\kappa+y)^2}\right], \tag{40}$$

one has

$$\Psi'(y) = \alpha\{\mathcal{R}'(y) - \rho\} - \{M(y) + yM'(y)\}(1 + \delta y) - \delta y M(y), \tag{41}$$

where $M'(y) = \mathcal{R}'(y) + \rho$. This is a sufficient parameter-screening criterion, not a general uniqueness theorem.

For the reference values

$$\begin{aligned} &\alpha = 5.1523, \quad \beta = 0.2857, \quad \gamma = 25.6739, \quad s = 1.5179, \\ &\lambda = 3.4018, \quad \kappa = 0.3591, \quad \rho = 0.5088, \quad \delta = 3.4386, \end{aligned} \tag{42}$$

condition (39) does not hold globally. Numerical root isolation on $[0, y_{\max}]$, with $y_{\max} = 1.08727804$, gives one zero,

$$E^* = (0.03677290,\ 1.08249054). \tag{43}$$

The two numerically located stationary points of Ψ occur near $y = 0.0097516$ and $y = 0.7426721$, where Ψ remains positive; the single zero occurs after the second stationary point. Accordingly, uniqueness for this reference set is numerical evidence, whereas only existence and the conditional criterion are analytical results. Figure 4 gives the corresponding nullclines.

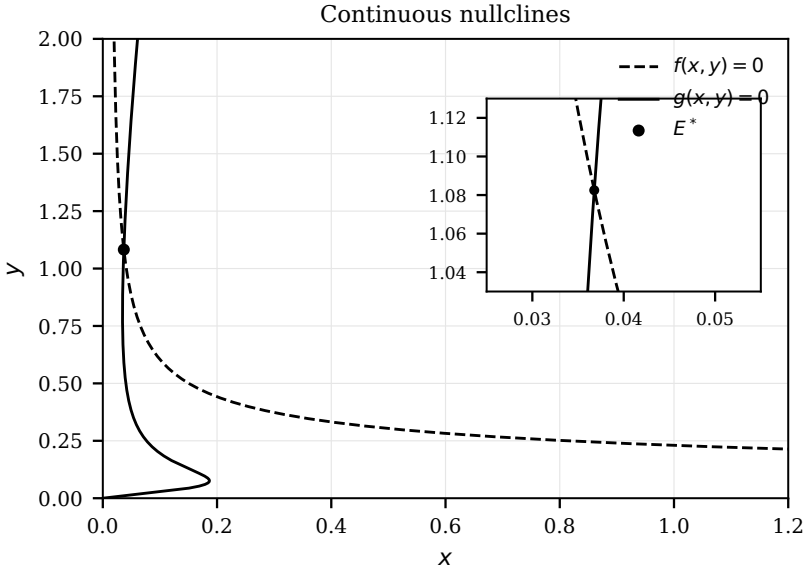

Figure 4. Nullclines of the continuous model for (42). The inset magnifies the numerically isolated positive equilibrium.

The scalar equation also connects directly to the full Jacobian. Along

the $f = 0$ nullcline, $x(y) = \alpha/M(y)$ and $g(x(y), y) = \Psi(y)/M(y)$. At a positive equilibrium,

$$\frac{d}{dy}g(x(y), y) = \frac{\Psi'(y^*)}{M(y^*)} = \frac{\det J_c(E^*)}{f_x(E^*)} = -\frac{\det J_c(E^*)}{M(y^*)}. \tag{44}$$

Hence

$$\boxed{\det J_c(E^*) = -\Psi'(y^*)}. \tag{45}$$

Therefore the scalar saddle-node condition $\Psi'(y^*) = 0$ is exactly the zero-eigenvalue condition of the two-dimensional linearization.

7 Local stability of the continuous model

The Jacobian matrix of (20)–(21) is

$$J_c(x, y) = \begin{pmatrix} -M(y) & -x\{\mathcal{R}'(y) + \rho\} \\ Q(y) - \rho y & x\mathcal{R}'(y) - 1 - \rho x - 2\delta y \end{pmatrix}. \tag{46}$$

The continuous Jacobian (46) is the basis for the trace-determinant stability criteria below. At an equilibrium E^* define

$$T_c = \operatorname{tr} J_c(E^*), \qquad D_c = \det J_c(E^*). \tag{47}$$

The characteristic polynomial is

$$\xi^2 - T_c\xi + D_c = 0. \tag{48}$$

Hence the standard trace-determinant classification gives the following criterion.

Proposition 5 (Local stability)**.** *A positive equilibrium E^* of* (20)–(21) *is locally asymptotically stable if*

$$T_c < 0, \qquad D_c > 0. \tag{49}$$

It is a saddle if $D_c < 0$. If $D_c > 0$ and $T_c > 0$, it is unstable. Non-hyperbolicity occurs when $D_c = 0$, or when $T_c = 0$ and $D_c > 0$. The

equality $T_c^2 - 4D_c = 0$ only indicates repeated eigenvalues and does not, by itself, imply loss of hyperbolicity.

Proof. The linearization of the system at E^* is $U' = J_c(E^*)U$, where $U = (x - x^*, y - y^*)^T$. The characteristic polynomial of $J_c(E^*)$ is

$$\chi(\xi) = \xi^2 - T_c\xi + D_c. \tag{50}$$

For a second-order real polynomial $\xi^2 + a_1\xi + a_0$, the Routh–Hurwitz criterion gives negative real parts of both roots if and only if $a_1 > 0$ and $a_0 > 0$. Here $a_1 = -T_c$ and $a_0 = D_c$. Therefore both eigenvalues have negative real parts exactly when $T_c < 0$ and $D_c > 0$, and the equilibrium is locally asymptotically stable by the linearization theorem. If $D_c < 0$, the product of the two eigenvalues is negative, so the eigenvalues are real with opposite signs and the equilibrium is a saddle. If $D_c > 0$ and $T_c > 0$, the sum of the eigenvalues has positive real part; either both real parts are positive or the complex conjugate pair has positive real part, so the equilibrium is unstable. Finally, $D_c = 0$ gives a zero eigenvalue. If $T_c = 0$ and $D_c > 0$, the eigenvalues are $\xi_{1,2} = \pm i\sqrt{D_c}$ and have zero real part, which is the Hopf-type non-hyperbolic case for the planar flow. A repeated eigenvalue occurs when $T_c^2 - 4D_c = 0$; such a repeated eigenvalue may still be hyperbolic if its real part is non-zero, and therefore this discriminant condition is not a general non-hyperbolicity condition. ■

The stability condition has a direct chemical reading. The diagonal entry $-M(y^*)$ is always negative and represents consumption of A through background conversion, autocatalysis, and quenching. The second diagonal entry,

$$x^*\mathcal{R}'(y^*) - 1 - \rho x^* - 2\delta y^*, \tag{51}$$

compares local autocatalytic feedback with first-order decay, cross-quenching, and nonlinear termination. Stability loss requires the feedback derivative $x^*\mathcal{R}'(y^*)$ to become large enough relative to the loss terms.

8 Continuous-time bifurcation analysis

Proposition 6 (Simple-zero saddle-node criterion)**.** *Let ν be a scalar parameter. Suppose that a positive equilibrium (x^*, y^*) at $\nu = \nu_0$ satisfies*

$$\Psi(y^*; \nu_0) = 0, \qquad \Psi_y(y^*; \nu_0) = 0, \tag{52}$$

and

$$\Psi_{yy}(y^*; \nu_0) \neq 0, \qquad \Psi_\nu(y^*; \nu_0) \neq 0, \qquad T_c(E^*; \nu_0) \neq 0. \tag{53}$$

Then the equilibrium undergoes a generic saddle-node bifurcation as ν passes through ν_0.

Proof. Because $f_x(E^*) = -M(y^*) < 0$, the equation $f = 0$ defines the smooth nullcline $x = x(y, \nu) = \alpha/M(y, \nu)$ locally. Along this nullcline,

$$h(y, \nu) := g(x(y, \nu), y, \nu) = \frac{\Psi(y, \nu)}{M(y, \nu)}.$$

At a point satisfying (52),

$$h_y = 0, \qquad h_{yy} = \frac{\Psi_{yy}}{M} \neq 0, \qquad h_\nu = \frac{\Psi_\nu}{M} \neq 0.$$

Furthermore, (45) gives $D_c = 0$, while $T_c \neq 0$ ensures that the zero eigenvalue is simple. The one-dimensional center-manifold reduction therefore has the nondegenerate saddle-node normal form. ∎

The trace condition in (53) excludes a double-zero degeneracy. The parameter ν may be α, γ, λ, ρ, δ, or another scalar control parameter.

Proposition 7 (Nondegenerate Hopf criterion)**.** *Suppose that a smooth equilibrium branch $E^*(\nu)$ satisfies*

$$T_c(E^*; \nu_0) = 0, \qquad D_c(E^*; \nu_0) > 0, \tag{54}$$

and

$$\frac{d}{d\nu} T_c(E^*(\nu); \nu)\Big|_{\nu=\nu_0} \neq 0. \tag{55}$$

If the first Lyapunov coefficient in (58) *is nonzero, then a nondegenerate Hopf bifurcation occurs at* ν_0*. Under the convention used below,* $l_1 < 0$ *gives locally attracting periodic orbits on the side where the equilibrium is unstable.*

Proof. Since $D_c > 0$, the equilibrium continues smoothly with ν. At $T_c = 0$, the eigenvalues are the simple pair $\pm i\omega_0$, where $\omega_0 = \sqrt{D_c}$. Their real part is $T_c/2$, so (55) is the eigenvalue-crossing condition. The conclusion follows from the Hopf bifurcation theorem when $l_1 \neq 0$ [19, 23]. ■

Let $A = J_c(E^*)$, let q be a right eigenvector of A corresponding to $i\omega_0$, and let p be a right eigenvector of A^T corresponding to $-i\omega_0$. The Hermitian product $\langle p, q\rangle = \bar{p}^T q$ is used. To remove the scaling ambiguity, the computations impose $\|q\|_2 = 1$ and then scale p so that $\langle p, q\rangle = 1$. For perturbation vectors $u, v, w \in \mathbb{C}^2$, the non-zero multilinear terms are

$$\begin{aligned} B_1(u,v) &= -\{\mathcal{R}'(y^*) + \rho\}(u_1 v_2 + u_2 v_1) - x^* \mathcal{R}''(y^*) u_2 v_2, \\ B_2(u,v) &= \{\mathcal{R}'(y^*) - \rho\}(u_1 v_2 + u_2 v_1) + \{x^* \mathcal{R}''(y^*) - 2\delta\} u_2 v_2, \end{aligned} \tag{56}$$

and

$$\begin{aligned} C_1(u,v,w) = &-\mathcal{R}''(y^*)(u_1 v_2 w_2 + u_2 v_1 w_2 + u_2 v_2 w_1) \\ &- x^* \mathcal{R}'''(y^*) u_2 v_2 w_2, \\ C_2(u,v,w) = &\,\mathcal{R}''(y^*)(u_1 v_2 w_2 + u_2 v_1 w_2 + u_2 v_2 w_1) \\ &+ x^* \mathcal{R}'''(y^*) u_2 v_2 w_2. \end{aligned} \tag{57}$$

These definitions use the Taylor convention $F(U) = AU + \frac{1}{2}B(U,U) + \frac{1}{6}C(U,U,U) + O(\|U\|^4)$. The first Lyapunov coefficient is

$$\begin{aligned} l_1 = \frac{1}{2\omega_0} \operatorname{Re} \Big\langle p, &C(q, q, \bar{q}) - 2B(q, A^{-1} B(q, \bar{q})) \\ &+ B\{\bar{q}, (2i\omega_0 I - A)^{-1} B(q, q)\} \Big\rangle. \end{aligned} \tag{58}$$

The derivatives entering B and C were evaluated analytically from (23)–(24). Complex linear systems and inner products in (58) were evaluated in IEEE double precision under the normalization $\|q\|_2 = 1$ and $\langle p, q\rangle =$

1. The magnitude of l_1 depends on the normalization, whereas its sign determines the local criticality.

Consider the parameter family

$$\beta = 0.2, \quad \gamma = 15, \quad s = 1, \quad \lambda = 2.5, \quad \kappa = 0.4, \quad \rho = 0.3, \quad \delta = 0.5, \tag{59}$$

with α as the bifurcation parameter. A logarithmic scan over $10^{-7} \leq \alpha \leq 10^4$, supplemented by a dense linear scan on $0.05 \leq \alpha \leq 0.30$, isolates the two trace crossings in Table 2. Bracketed scalar root refinement used absolute tolerance 10^{-12}.

Table 2. Continuous-time Hopf points for the parameter family (59).

Point	α	(x^*, y^*)	ω_0	$\mathrm{d}T_c/\mathrm{d}\alpha$	l_1
H_1	0.148614	$(0.229890, 0.123859)$	0.820902	3.56235	-18.3333
H_2	0.187434	$(0.191731, 0.157038)$	1.015675	-3.40993	-15.6854

The nonzero trace derivatives verify transversality. The negative first Lyapunov coefficients establish supercritical Hopf bifurcations under the normalization in (58). The equilibrium is unstable for $H_1 < \alpha < H_2$. In a neighbourhood of each Hopf point, the bifurcating periodic orbit lies on the unstable-equilibrium side and is locally attracting. The local calculation does not, by itself, prove that a single periodic branch connects H_1 and H_2. Figure 5 shows the trace and the equilibrium y-coordinate on the displayed part of the branch.

9 Continuous simulations

The continuous trajectories were computed with the adaptive Dormand–Prince DOP853 method, relative tolerance 10^{-11}, absolute tolerance 10^{-13}, maximum step 10^{-3}, IEEE double precision, and initial state $(x(0), y(0)) = (0.4, 0.05)$. Figure 6 compares a stable focus and a Hopf-generated oscillatory response. The stable case approaches the positive equilibrium after a damped transient, whereas the second trajectory approaches a small attracting cycle.

Figure 7 displays the local vector field and the attracting periodic or-

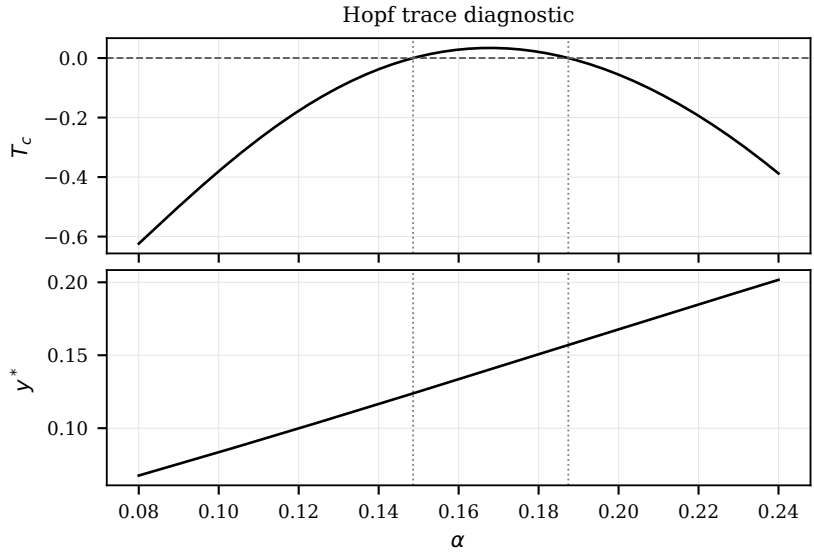

Figure 5. Continuous-time Hopf diagnostic for (59). The zero crossings of T_c mark the Hopf points listed in Table 2.

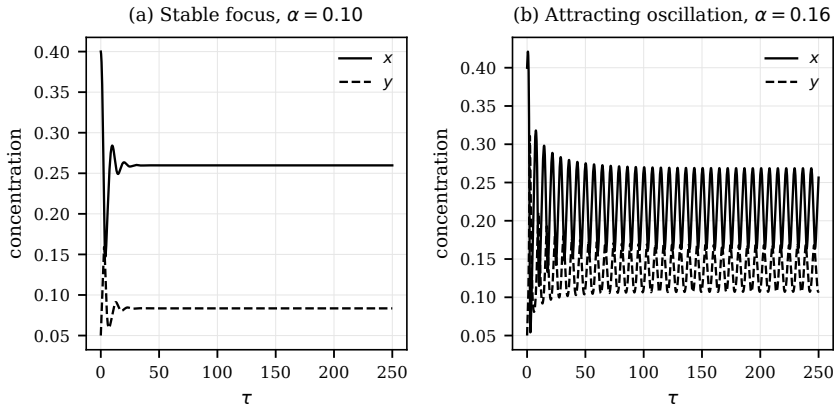

Figure 6. Continuous-time concentration responses. Left: stable focus for $\alpha = 0.10$; right: Hopf-generated oscillation for $\alpha = 0.16$, with the solver settings and initial state stated in the text.

bit for $\alpha = 0.16$. The trajectory remains in the positive quadrant, and the oscillation is generated by the balance between thermal autocatalytic acceleration and damping by cross-quenching and termination.

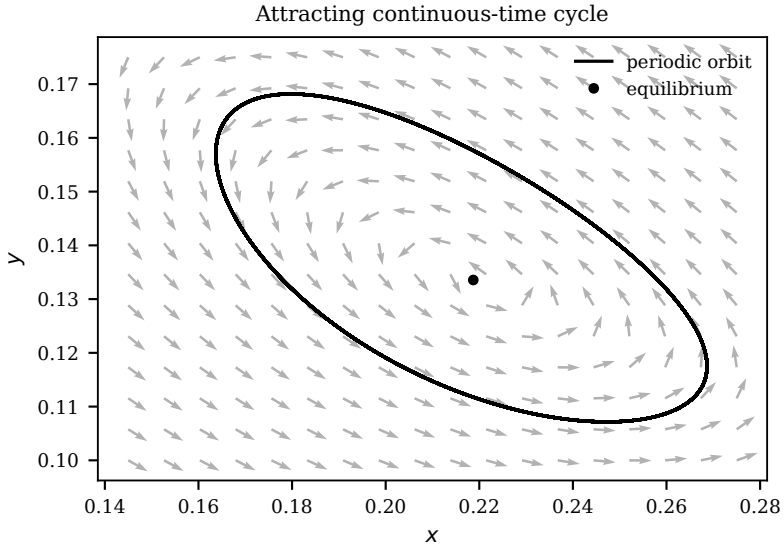

Figure 7. Phase-plane view of the attracting continuous-time cycle for $\alpha = 0.16$ in (59). Arrows show the normalized vector field.

These simulations display stable and oscillatory regimes of the two-intermediate flow. They do not imply deterministic chaos, which is excluded for bounded trajectories of the autonomous planar system. The discretization analysis below examines how a positive numerical update departs from this continuous dynamics as the step increases.

10 Reaction–diffusion extension and pattern formation

Let $\Omega \subset \mathbb{R}^2$ be a bounded, connected domain with C^2 boundary. The reaction–diffusion extension is

$$\frac{\partial X}{\partial \tau} = D_x \Delta X + f(X, Y), \qquad \frac{\partial Y}{\partial \tau} = D_y \Delta Y + g(X, Y), \tag{60}$$

with homogeneous no-flux conditions

$$\frac{\partial X}{\partial \mathbf{n}} = \frac{\partial Y}{\partial \mathbf{n}} = 0 \qquad \text{on } \partial\Omega, \tag{61}$$

where $D_x, D_y > 0$ are dimensionless diffusivities and $\mathbf{n}$ is the outward unit normal. The capital letters distinguish concentration fields from the well-mixed variables. Every kinetic equilibrium $E^* = (x^*, y^*)$ induces the homogeneous solution $(X, Y) \equiv E^*$.

Proposition 8 (Global well-posedness and positivity)**.** *Let* $(X_0, Y_0) \in C(\overline{\Omega}; \mathbb{R}^2_+)$. *System* (60)–(61) *has a unique global non-negative mild solution in* $C([0,\infty); C(\overline{\Omega})^2)$. *The solution is classical for* $\tau > 0$ *and is ultimately bounded in* $L^\infty(\Omega)^2$. *If the initial data have the usual parabolic regularity and satisfy the Neumann compatibility conditions, the solution is classical up to* $\tau = 0$.

Proof. The reaction vector is locally Lipschitz in a neighbourhood of the non-negative quadrant, so standard semilinear parabolic theory gives a unique local mild solution and the usual continuation alternative [20]. On the coordinate axes, $f(0, Y) = \alpha > 0$ and $g(X, 0) = \beta X \geq 0$. Quasipositivity and the parabolic maximum principle therefore preserve non-negativity. Moreover,

$$X_\tau - D_x \Delta X \leq \alpha - \beta X. \tag{62}$$

For every $\varepsilon > 0$, scalar comparison gives a time T_1 such that $\|X(\cdot, \tau)\|_\infty \leq X_\varepsilon := \alpha/\beta + \varepsilon$ for $\tau \geq T_1$. Because $0 \leq \mathcal{R}(Y) \leq R_{\max}$,

$$Y_\tau - D_y \Delta Y \leq X_\varepsilon(\beta + R_{\max}) - \delta Y^2, \qquad \tau \geq T_1. \tag{63}$$

Comparison with the corresponding scalar Riccati equation yields an ultimate L^∞ bound for Y. The two bounds exclude finite-time blow-up in the continuation alternative and hence extend the solution globally. Parabolic regularization gives classical smoothness for positive time. ∎

This result establishes chemical admissibility of the spatial model; it does not imply diffusion-driven instability.

10.1 Finite-domain Turing criterion

Let

$$J_c(E^*) = \begin{pmatrix} a_{11} & a_{12} \\ a_{21} & a_{22} \end{pmatrix}, \qquad \mathcal{D} = \operatorname{diag}(D_x, D_y), \tag{64}$$

where, from (46),

$$a_{11} = -M(y^*) < 0, \qquad a_{22} = x^* \mathcal{R}'(y^*) - 1 - \rho x^* - 2\delta y^*. \tag{65}$$

Let $0 = \mu_0 < \mu_1 \le \mu_2 \le \cdots$ be the eigenvalues of $-\Delta$ under (61). The linearization in the mode associated with μ_k is

$$J_k = J_c(E^*) - \mu_k \mathcal{D}. \tag{66}$$

Proposition 9 (Finite-domain diffusion-driven instability)**.** *Assume that E^* is asymptotically stable for the well-mixed kinetics, so that $T_c < 0$ and $D_c > 0$. Define*

$$\mathcal{A}_D = D_y a_{11} + D_x a_{22}. \tag{67}$$

Then E^* is linearly unstable to a non-constant Neumann mode if and only if there is an index $k \ge 1$ such that

$$P(\mu_k) := D_c - \mathcal{A}_D \mu_k + D_x D_y \mu_k^2 < 0. \tag{68}$$

A non-empty interval of unstable Laplacian spectral values exists precisely when

$$\mathcal{A}_D > 0, \qquad \mathcal{A}_D^2 > 4 D_x D_y D_c. \tag{69}$$

Under (69)*, condition* (68) *is equivalent to the requirement that at least one non-zero Neumann eigenvalue lie in*

$$\mu_- < \mu_k < \mu_+, \qquad \mu_\pm = \frac{\mathcal{A}_D \pm \sqrt{\mathcal{A}_D^2 - 4 D_x D_y D_c}}{2 D_x D_y}. \tag{70}$$

Proof. For mode k,

$$\operatorname{tr} J_k = T_c - (D_x + D_y)\mu_k < 0 \tag{71}$$

and direct expansion gives $\det J_k = P(\mu_k)$. Since the trace is negative, the mode has an eigenvalue with positive real part exactly when its determinant is negative. The quadratic P is strictly convex, satisfies $P(0) = D_c > 0$, and has positive leading coefficient. It is negative on a positive interval if and only if its vertex lies at a positive value of μ and its minimum is negative. These two requirements are exactly (69); solving $P(\mu) = 0$ then gives (70). On a bounded domain, instability additionally requires an admissible eigenvalue in this open interval. ■

Because $a_{11} < 0$, the first inequality in (69) forces $a_{22} > 0$ and

$$\frac{D_x}{D_y} > \frac{-a_{11}}{a_{22}}. \tag{72}$$

Thus Y must act locally as the self-enhancing component, while the precursor-like field X must diffuse sufficiently faster. This is the activator–substrate interpretation of the present mechanism. The condition is not satisfied by the stiff reference set (42), for which both a_{11} and a_{22} are negative. Pattern calculations based on that set would therefore contradict the linear theory.

For the square $\Omega = (0, 20)^2$, the Neumann eigenvalues are

$$\mu_{mn} = \frac{\pi^2(m^2 + n^2)}{400}, \qquad m, n = 0, 1, 2, \ldots. \tag{73}$$

Figure 8 gives the dispersion relation for the parameter family (59) at $\alpha = 0.14$, $D_x = 1$, and $D_y = 0.05$. Here $(T_c, D_c) = (-0.0376513, 0.614461)$ and the well-mixed equilibrium is stable, but (70) gives $1.3544 < \mu < 9.0734$. At fixed $D_x = 1$, the continuous-spectrum threshold occurs at $D_x/D_y \approx 10.13$; the displayed choice has ratio 20. The threshold is conditional on the phenomenological kinetics and must not be interpreted as a measured chemical diffusivity ratio.

10.2 Numerical pattern protocol

Three ODE-stable cases are used to illustrate distinct spatial organizations. The common kinetic parameters are those in (59); only α and D_y

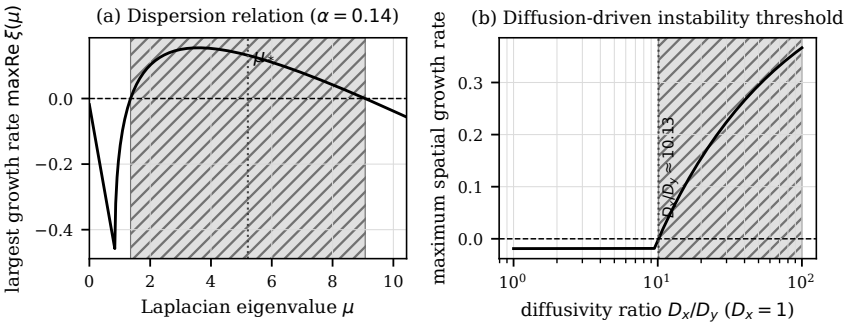

Figure 8. Linear diffusion-driven instability diagnostic for the family (59) at $\alpha = 0.14$. (a) Largest modal growth rate as a function of the Laplacian eigenvalue. The hatched interval is the analytical band (70), and the dotted line marks its vertex $\mu_* = \mathcal{A}_D/(2D_xD_y)$. (b) Maximum growth rate over the continuous Laplacian spectrum as D_x/D_y varies with $D_x = 1$. Hatching denotes the unstable side of the threshold. Only black, white, and grayscale elements are used.

vary, while $D_x = 1$. Their trace–determinant values are

$$\begin{array}{c|ccc} & \text{P1} & \text{P2} & \text{P3} \\ \hline T_c & -0.177315 & -0.0376513 & -0.194006 \\ D_c & 0.500478 & 0.614461 & 1.457943 \end{array} . \tag{74}$$

Hence the homogeneous mode is stable in every case. The corresponding diffusion bands and initial perturbations are listed in Table 3.

Table 3. Parameter cases used for the reaction–diffusion simulations. Here $D_x = 1$, $\Omega = (0, 20)^2$, and the remaining kinetic parameters are fixed by (59).

Case	α	(x^*, y^*)	D_y	(μ_-, μ_+)	Initial perturbation
P1	0.12	$(0.253208, 0.099846)$	0.025	$(2.1716, 9.2186)$	broadband random
P2	0.14	$(0.237907, 0.116567)$	0.050	$(1.3544, 9.0734)$	stripe mode $(15, 0)$
P3	0.22	$(0.163315, 0.184813)$	0.100	$(1.7232, 8.4606)$	square modes $(10, 0), (0, 10)$

The square was discretized on a cell-centred 128×128 grid with spacing $\Delta\zeta = 20/128$. Time integration used Strang splitting with step $\Delta\tau = 0.02$ up to $\tau = 600$. Each half diffusion step was evaluated exactly for the finite-difference Neumann Laplacian by an orthonormal discrete cosine transform; the pointwise reaction step used classical fourth-order Runge–

Kutta. The discrete non-negative Laplacian eigenvalues used by the diffusion solver were

$$\widehat{\mu}_{mn} = \frac{4}{(\Delta\zeta)^2}\left\{\sin^2\left(\frac{m\pi}{2N}\right) + \sin^2\left(\frac{n\pi}{2N}\right)\right\}, \qquad N = 128. \tag{75}$$

No clipping or positivity projection was applied. The smallest concentrations recorded over the saved times were $X = 0.02939$, $Y = 0.02673$ for P1; $X = 0.07475$, $Y = 0.04560$ for P2; and $X = 0.08157$, $Y = 0.08063$ for P3.

P1 starts from independent mean-zero Gaussian perturbations of relative standard deviation 10^{-2}, using seed 1729. P2 uses opposite relative perturbations of X and Y proportional to $10^{-2}\cos(15\pi\zeta_1/20)$. P3 uses opposite relative perturbations proportional to

$$\frac{10^{-2}}{2}\left\{\cos\left(\frac{10\pi\zeta_1}{20}\right) + \cos\left(\frac{10\pi\zeta_2}{20}\right)\right\}. \tag{76}$$

Thus P2 and P3 test the nonlinear evolution of specified unstable modes; only P1 tests selection from broadband noise.

Figure 9 records the growth and nonlinear saturation of spatial variance. P2 undergoes a long oscillatory reorganization before settling toward a coarser stripe state, whereas P1 and P3 reach their final amplitudes more directly. Over the last ten time units, the relative changes in the spatial standard deviation of Y are 2.11×10^{-5}, 1.04×10^{-3}, and 4.57×10^{-10} for P1–P3, respectively. P2 is therefore described as near-stationary at the reported final time, not as a numerically proved asymptotic steady state.

Refinement calculations used the baseline $(N, \Delta\tau) = (128, 0.02)$, the half-step case $(128, 0.01)$ and the finer-grid case $(192, 0.02)$. Table 4 summarizes the final autocatalyst fields.

Table 4. Reaction–diffusion refinement at $\tau = 600$. Each entry lists the final standard deviation of Y and its dominant discrete mode.

Case	$(128, 0.02)$	$(128, 0.01)$	$(192, 0.02)$
P1	0.14204, $(0, 18)$	0.14303, $(0, 16)$	0.14131, $(0, 16)$
P2	0.09252, $(10, 0)$	0.09067, $(8, 0)$	0.09188, $(9, 0)$
P3	0.08420, $(10, 10)$	0.08436, $(10, 10)$	0.08401, $(10, 10)$

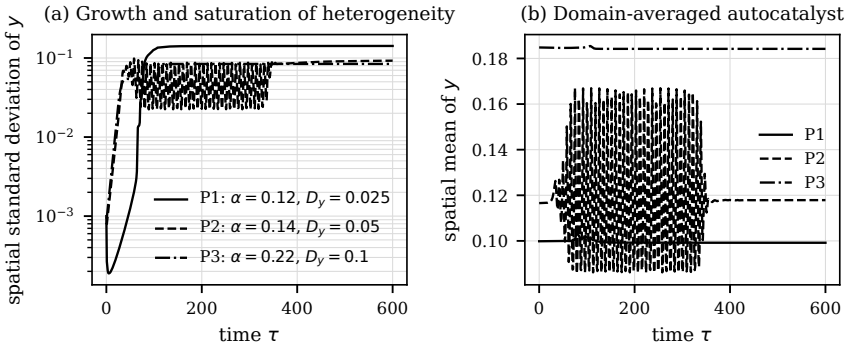

Figure 9. Finite-time formation diagnostics for P1–P3. (a) Growth and saturation of the spatial standard deviation of the autocatalyst field. (b) Evolution of its domain average. Line styles, rather than color, distinguish the cases.

P3 is stable under both refinements: after interpolation to a common grid, the relative field differences are 8.9×10^{-4} and 1.5×10^{-2} for the half-step and fine-grid calculations. P1 and P2 preserve their morphology and amplitude but not their final dominant wavelength. For P2, the corresponding one-dimensional profile differences are 0.905 and 0.084 relative to the baseline. For P1, the fine-grid calculation uses a different grid-level realization of the prescribed random noise, so a pointwise field difference is not meaningful; the amplitude and spot morphology remain comparable. These results establish numerical convergence for P3 only. P1 and P2 are finite-time examples of pattern formation, not converged wavelength predictions.

The final fields in Figure 10 show three organizations: a noise-selected irregular spot lattice (P1), a mode-selected stripe state after wavelength coarsening (P2), and a square-symmetric spot–depletion lattice (P3). In each pair, precursor and autocatalyst deviations are predominantly out of phase, consistent with local precursor depletion around autocatalyst-rich regions. The plots show deviations from the corresponding equilibrium, not absolute concentrations; separate symmetric grayscale ranges are used because the three cases have different amplitudes.

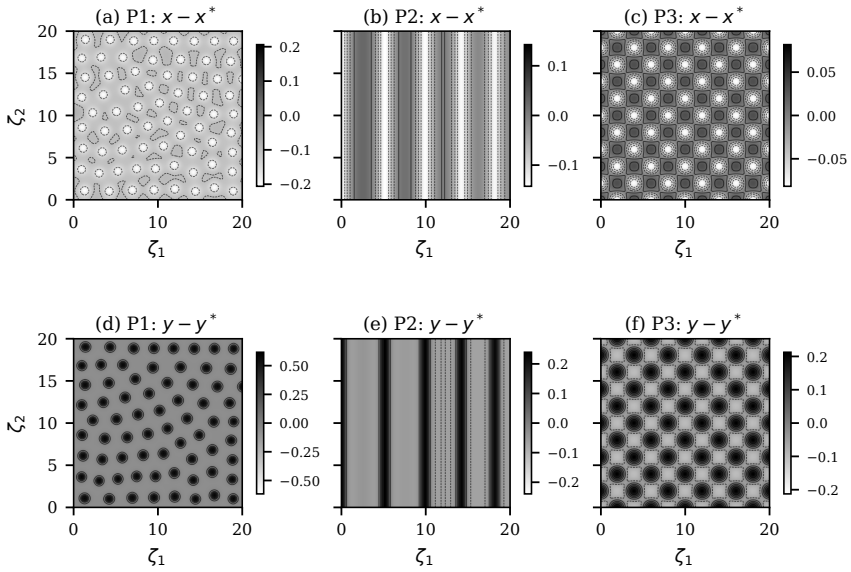

Figure 10. Black-and-white spatial fields at $\tau = 600$. Panels (a)–(c) show $X - x^*$, and panels (d)–(f) show $Y - y^*$, for cases P1–P3 in Table 3. P1 is initialized by broadband noise, whereas P2 and P3 use the stated mode-selected perturbations. Grayscale shading is supplemented by black contours to preserve structure in print.

10.3 Interpretation, importance, and limitations

The spatial analysis adds a mechanism that is absent from the well-mixed model: differential transport can select an intrinsic length scale even though the zero-wave-number equilibrium is stable. This matters chemically because localized autocatalyst-rich regions can coexist with precursor-depleted regions without invoking a temporally unstable homogeneous reactor. The analytical band (70) also separates a proved linear statement from the nonlinear numerical evidence: it predicts which infinitesimal modes grow, whereas the ultimate spot or stripe morphology depends on nonlinear mode competition, the domain, and the initial perturbation.

The calculations are conditional demonstrations, not quantitative predictions for a named reaction. The diffusivities have not been measured, the no-flux square is an idealized geometry, and no weakly nonlinear am-

plitude equation or global nonlinear stability theorem is claimed. In particular, the three panels do not constitute an exhaustive morphology diagram. Experimental use would require independently estimated diffusion coefficients, reactor geometry and boundary exchange, calibration of the thermal closure, and comparison of the observed wavelength with (70).

11 A positive semi-implicit discretization

To approximate (20)–(21) over a numerical step $h > 0$, consider the semi-implicit update

$$x_{n+1} = F_1(x_n, y_n) = \frac{x_n + h\alpha}{1 + h\{\beta + \mathcal{R}(y_n) + \rho y_n\}}, \tag{77}$$

$$y_{n+1} = F_2(x_n, y_n) = \frac{y_n + h\{\beta + \mathcal{R}(y_n)\}x_n}{1 + h\{1 + \rho x_n + \delta y_n\}}. \tag{78}$$

Production terms are evaluated explicitly and the principal loss terms are placed in the denominators. This construction preserves non-negative concentrations for every $h > 0$, in the spirit of nonstandard and positivity-preserving finite-difference methods [1,2,8,9,26,27,29,31]. Equations (77)–(78) are treated only as a numerical discretization. They are not derived from pulsing, dilution, residence-time resetting, or an exact stroboscopic chemical protocol.

Proposition 10 (Positivity, fixed points, and consistency)**.** *Map* (77)–(78) *maps* $\mathbb{R}^2_+$ *into* $\mathbb{R}^2_+$*, has exactly the same positive fixed points as the continuous model, and is first-order consistent:*

$$F(x, y; h) = \begin{pmatrix} x \\ y \end{pmatrix} + h \begin{pmatrix} f(x, y) \\ g(x, y) \end{pmatrix} + O(h^2) \qquad (h \to 0) \tag{79}$$

uniformly on compact subsets of $\mathbb{R}^2_+$*.*

Proof. For $x, y \geq 0$, the numerators and denominators in (77)–(78) are positive. A fixed point satisfies

$$\alpha = x^*\{\beta + \mathcal{R}(y^*) + \rho y^*\}, \qquad \{\beta + \mathcal{R}(y^*)\}x^* = y^* + \rho x^* y^* + \delta(y^*)^2, \tag{80}$$

which is equivalent to $f(x^*, y^*) = g(x^*, y^*) = 0$. Conversely, every equilibrium of the flow satisfies the fixed-point equations. Finally, expanding $(1+ha)^{-1} = 1-ha+O(h^2)$ in each component gives the stated first-order consistency. ∎

Proposition 11 (Discrete absorbing estimate)**.** *Assume $s > 0$ and $\delta > 0$. For every fixed $h > 0$, map (77)–(78) admits an absorbing rectangle in $\mathbb{R}^2_+$.*

Proof. Since $\mathcal{R}(y) \geq 0$ and $\rho y \geq 0$,

$$0 \leq x_{n+1} \leq \frac{x_n + h\alpha}{1 + h\beta}. \tag{81}$$

The comparison recurrence has the attracting fixed value α/β. Thus, for every $\varepsilon > 0$, there is N_1 such that $x_n \leq X_\varepsilon := \alpha/\beta + \varepsilon$ for $n \geq N_1$. Since $\mathcal{R}(y) \leq R_{\max} := (\gamma/s)e^{\lambda}$, define $A_\varepsilon = X_\varepsilon(\beta + R_{\max})$. For $n \geq N_1$,

$$y_{n+1} \leq H(y_n) := \frac{y_n + hA_\varepsilon}{1 + h + h\delta y_n}. \tag{82}$$

The scalar function H is bounded on $[0, \infty)$. For $0 \leq y \leq (h\delta)^{-1}$,

$$H(y) \leq \frac{(h\delta)^{-1} + hA_\varepsilon}{1 + h}, \tag{83}$$

whereas for $y > (h\delta)^{-1}$,

$$H(y) \leq \frac{1}{h\delta} + hA_\varepsilon. \tag{84}$$

These estimates provide a finite upper bound for all iterates after $N_1 + 1$ and hence an absorbing rectangle. ∎

12 Local Schur stability of the discretization

At a positive fixed point $E^* = (x^*, y^*)$, define

$$D_1 = 1 + hM(y^*), \qquad D_2 = 1 + h\{1 + \rho x^* + \delta y^*\}. \tag{85}$$

The fixed-point Jacobian is

$$J_d(E^*) = \begin{pmatrix} \dfrac{1}{D_1} & -\dfrac{hx^*\{\mathcal{R}'(y^*)+\rho\}}{D_1} \\ \dfrac{h\{Q(y^*)-\rho y^*\}}{D_2} & \dfrac{1+hx^*\mathcal{R}'(y^*)-h\delta y^*}{D_2} \end{pmatrix}. \tag{86}$$

Let $T_d = \operatorname{tr} J_d(E^*)$ and $\Delta_d = \det J_d(E^*)$.

Proposition 12 (Schur stability criterion)**.** *The fixed point E^* is locally asymptotically stable if and only if*

$$1 - T_d + \Delta_d > 0, \qquad 1 + T_d + \Delta_d > 0, \qquad 1 - \Delta_d > 0. \tag{87}$$

The respective equality boundaries correspond to a multiplier $+1$, a multiplier -1, and a complex unit-circle pair when $|T_d| < 2$. A full fold, period-doubling, or Neimark–Sacker theorem additionally requires transversality and the relevant non-degeneracy coefficient.

Proof. The characteristic polynomial is $\mu^2 - T_d\mu + \Delta_d$. Applying the Jury criterion for a monic quadratic gives (87). Substitution of $\mu = 1$ and $\mu = -1$ yields the first two boundaries. A non-real conjugate pair on the unit circle has product one, which gives $\Delta_d = 1$, while $|T_d| < 2$ excludes the real endpoints. ∎

The continuous and discrete local dynamics must be distinguished. If λ_1 and λ_2 are eigenvalues of $J_c(E^*)$, then the exact time-h flow map has multipliers $\exp(h\lambda_1)$ and $\exp(h\lambda_2)$. Consequently, a hyperbolic stable equilibrium of the differential equation remains stable under exact sampling for every $h > 0$. For the base set (42),

$$\lambda_1 \approx -133.2962, \qquad \lambda_2 \approx -8.8624. \tag{88}$$

The exact-flow multipliers therefore remain in $(0, 1)$ for every positive h. In contrast, the numerical map first satisfies $\Delta_d = 1$ at

$$h_c \approx 0.617496, \qquad \mu_{1,2} \approx 0.344775 \pm 0.938685i, \qquad |\mu_{1,2}| = 1. \tag{89}$$

The crossing is transversal, with

$$\frac{d}{dh}\max_i |\mu_i(h)|\Big|_{h=h_c} \approx 0.2068 > 0. \tag{90}$$

It is therefore the first local Schur-stability loss of the discrete fixed point. At $h = 4$, the multiplier modulus is approximately 1.13044 even though the continuous equilibrium remains strongly stable. Figure 11 compares the numerical multiplier with the exact sampled linearized flow. The boundary h_c concerns only the linearized fixed point; it is not an accuracy threshold for transient trajectories.

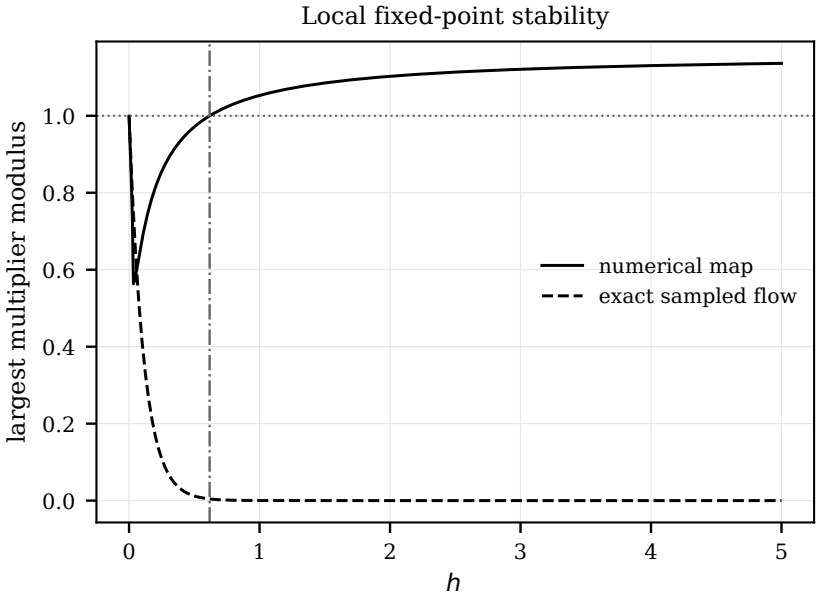

Figure 11. Local stability comparison for the base parameter set. The positivity-preserving scheme loses Schur stability at $h_c \approx 0.617496$ (vertical line), whereas the largest exact-flow multiplier $\max_i |e^{h\lambda_i}|$ remains below one for every $h > 0$.

13 Trajectory accuracy and step refinement

Local Schur stability and trajectory accuracy are different requirements. Let $Z_h(t_n)$ denote the numerical state after $n = t_n/h$ applications of (77)–(78), and let $Z_{\mathrm{ref}}(t)$ be a DOP853 reference solution computed with relative tolerance 10^{-11}, absolute tolerance 10^{-13}, and maximum step 10^{-3}. For $T = 1$, define

$$e(h,T) = \|Z_h(T) - Z_{\mathrm{ref}}(T)\|_2, \qquad E(h,T) = \max_{0 \le n \le T/h} \|Z_h(t_n) - Z_{\mathrm{ref}}(t_n)\|_2. \tag{91}$$

The initial condition is $(0.4, 0.3)$. The reference states are

$$\begin{aligned} Z_{\mathrm{ref}}(0.5) &= (0.03699805, 1.07793348), \\ Z_{\mathrm{ref}}(1) &= (0.03677556, 1.08243625). \end{aligned} \tag{92}$$

Although $h = 0.5 < h_c$, two map steps give

$$Z_{0.5}(1) = (0.04381198, 10.15268718), \qquad e(0.5, 1) = 9.07025. \tag{93}$$

Thus $h < h_c$ does not ensure an accurate transient approximation. Table 5 and Figure 12 show the refinement results. The maximum mesh error becomes asymptotically first order only for small steps; the observed orders over the five smallest successive refinements range from approximately 1.02 to 1.15.

Table 5. Selected step-refinement errors at $T = 1$.

h	$e(h,1)$	$E(h,1)$
0.500000	9.0703	9.0703
0.125000	6.0627×10^{-2}	2.5193
0.031250	6.2269×10^{-5}	8.0603×10^{-1}
0.0078125	6.2250×10^{-5}	1.6993×10^{-1}
0.0019531	1.8697×10^{-5}	3.7712×10^{-2}
0.0004883	4.8608×10^{-6}	9.1065×10^{-3}

The local fixed-point boundary h_c and the refinement errors answer different questions. The former identifies the first change in the type of the numerical fixed point, whereas (91) measures approximation of the

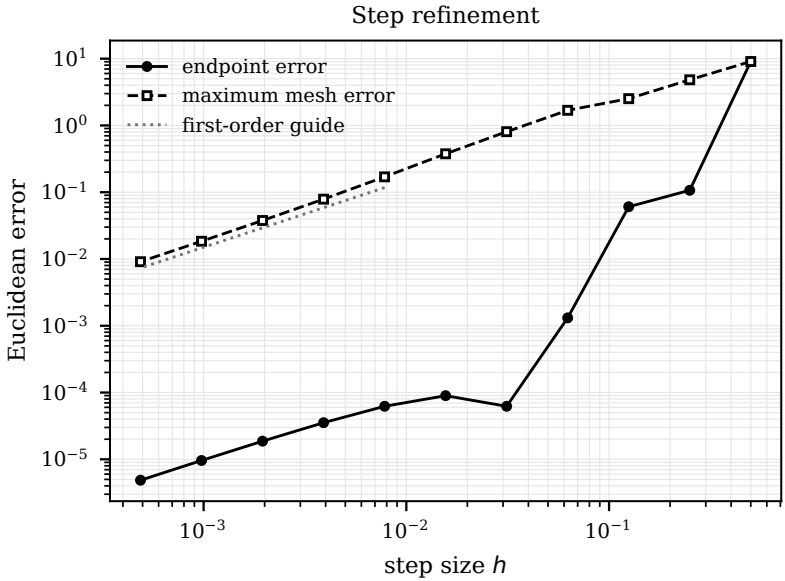

Figure 12. Endpoint and maximum mesh errors for $T = 1$. Coarse-step errors are non-monotone; the small-step branch approaches the expected first-order slope.

continuous trajectory over a specified time interval.

14 Numerical protocol

For orbitwise Lyapunov calculations the full Jacobian, not only (86), is required. Let

$$\begin{aligned} D_1(x, y) &= 1 + hM(y), \\ D_2(x, y) &= 1 + h(1 + \rho x + \delta y), \\ N_2(x, y) &= y + hQ(y)x. \end{aligned} \tag{94}$$

Then

$$DF(x,y)=\begin{pmatrix} \dfrac{1}{D_1} & -\dfrac{h(x+h\alpha)\{\mathcal{R}'(y)+\rho\}}{D_1^2} \\ \dfrac{hQ(y)D_2-h\rho N_2}{D_2^2} & \dfrac{\{1+hx\mathcal{R}'(y)\}D_2-h\delta N_2}{D_2^2} \end{pmatrix}. \tag{95}$$

The largest finite-time exponent per map iterate is computed as

$$L_1^{(N)}=\frac{1}{N}\sum_{n=0}^{N-1}\log\frac{\|DF(x_n,y_n)v_n\|_2}{\|v_n\|_2}, \tag{96}$$

with Euclidean norm, initial tangent vector $v_0=(1,0)^T$, and renormalization after every multiplication. The exponent is measured per iterate; division by h gives the value per unit dimensionless time. Computations use IEEE double precision. Positive finite-time values are reported as evidence of sensitive dynamics in the numerical map, not as proof of chaos in the differential equation.

Table 6. Numerical settings for the discrete calculations.

Calculation	Setting
Initial state	$(x_0,y_0)=(0.4,0.3)$ unless stated otherwise
Selected orbits	10 000 transients and 400 retained iterates
One-parameter scans	340 parameter values; 2500 transients, 120 plotted iterates and 2000 tangent updates
Two-parameter scans	140×140 grid, 1000 transients, and 1000 tangent updates
Tangent dynamics	$v_0=(1,0)^T$; full Jacobian (95); renormalization at every iterate
Period detection	180×180 initial-state grid; 5000 transients; 256 retained iterates; periods 1–64 tested over the last 96 pairs with tolerance 10^{-5}
Convergence check	$N=2000$, 5000, 10 000, and 100 000 after 10 000 transients
Units	$L_1^{(N)}$ per iterate; $L_1^{(N)}/h$ per unit dimensionless time
Interpretation	Positive converged value is evidence for the numerical map only

For the three representative step sizes, using 10 000 transient iterations

gives

h	$L_1^{(2000)}$	$L_1^{(5000)}$	$L_1^{(10000)}$
4	−0.00713	−0.00567	−0.00519
12	0.11550	0.12046	0.12433
12.9519	0.12010	0.11823	0.11968

(97)

The signs are stable under these accumulation lengths. Over 100 000 tangent updates, the estimates are 0.12777 for $h = 12$ and 0.11907 for $h = 12.9519$. Dividing the records into ten blocks of 10 000 updates gives standard errors 8.2×10^{-4} and 7.5×10^{-4}, respectively. The period-10 case has a small negative exponent, whereas the two coarse aperiodic cases retain positive exponents.

15 Coarse-step numerical responses

Figure 13 compares three numerical step sizes. At $h = 0.5 < h_c$, the fixed point is stable. At $h = 4$, the orbit converges to an attracting period-10 cycle and the largest finite-time Lyapunov exponent is slightly negative. At $h = 12.9519$, the retained orbit is aperiodic over the tested period range and has a positive finite-time exponent. These attractors belong to the discrete scheme; they are not trajectories of the autonomous planar flow.

Figure 15 shows the step-size bifurcation diagram together with $L_1^{(N)}$. The analytically computed threshold h_c is marked. Negative values identify attracting fixed or periodic responses, whereas positive windows identify sensitive discrete dynamics. The figure is a local fixed-point stability and finite-time response diagram. Crossing h_c proves loss of the equilibrium's Schur stability, but neither side of that boundary alone establishes trajectory accuracy.

At fixed $h = 12$, Figure 16 varies the autocatalytic strength γ. The resulting windows quantify how the numerical error interacts with the nonlinear kinetic scale. They do not imply that the continuous flow is chaotic for the same parameter values.

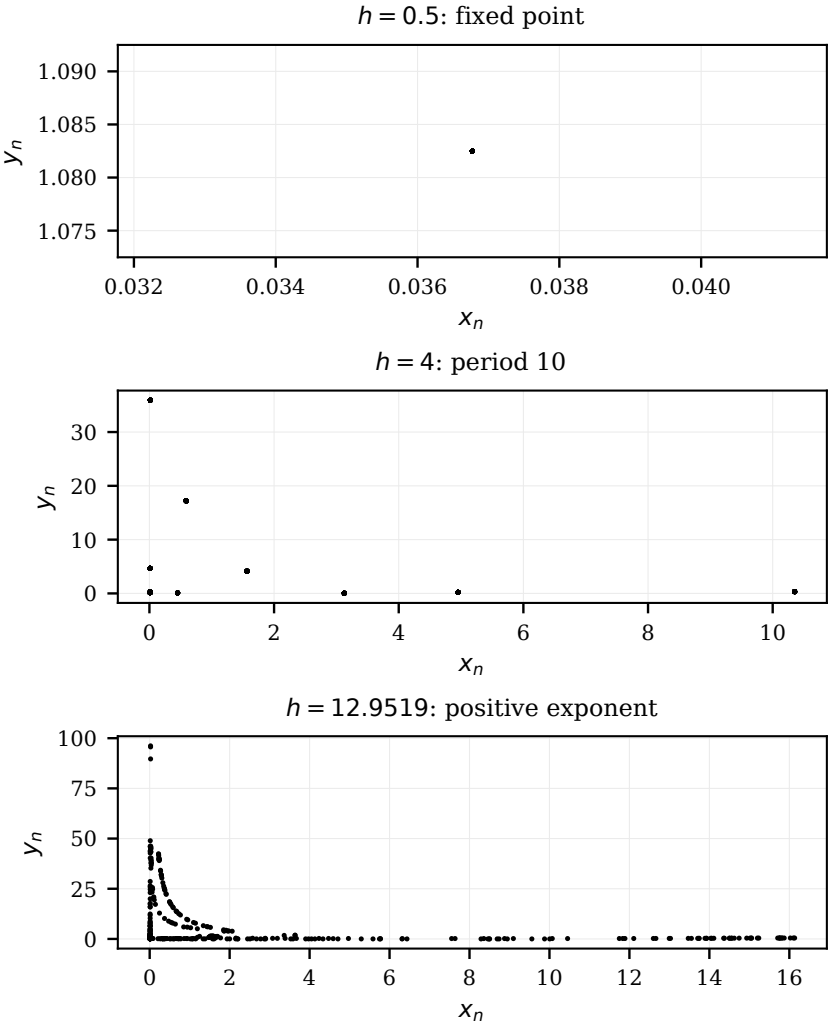

Figure 13. Representative numerical-map orbits for (42): fixed-point convergence at $h = 0.5$, an attracting period-10 cycle at $h = 4$, and an aperiodic positive-exponent response at $h = 12.9519$.

16 Two-parameter numerical diagrams

Figure 17 shows finite-time Lyapunov exponents on three 140×140 parameter grids. The zero contours are numerical classification boundaries, not

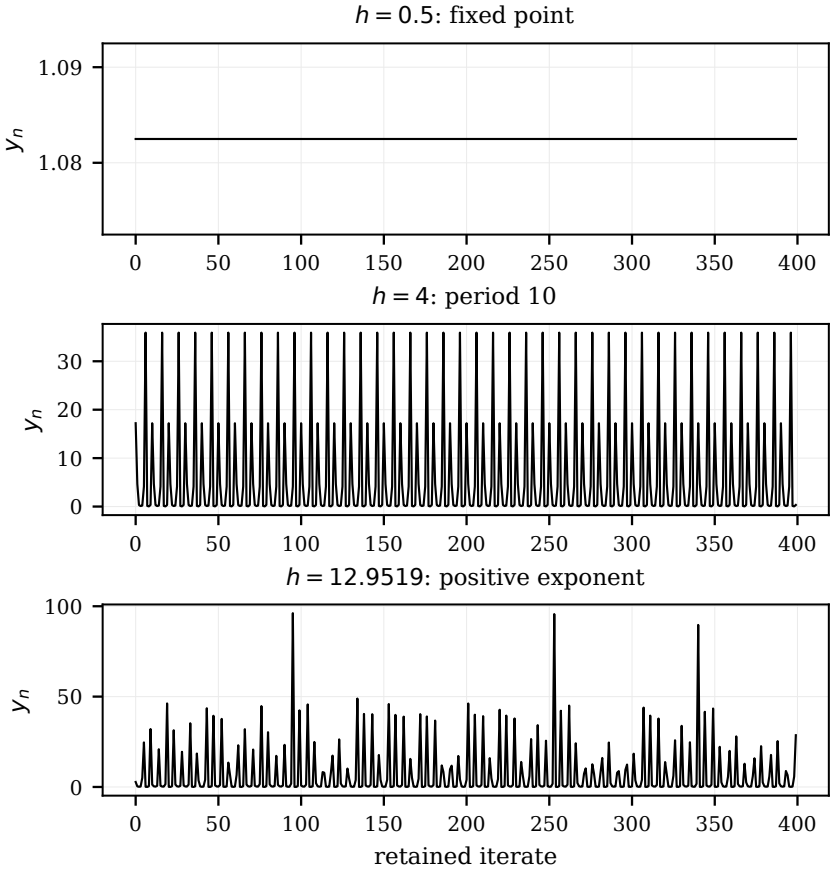

Figure 14. Autocatalyst iterates corresponding to Figure 13. The distinct vertical scales are retained to avoid compressing the fixed-point and period-10 regimes.

analytical bifurcation curves or chemical operating limits. The first two panels confirm that positive-exponent regions occur only when the numerical step is coarse. The third panel shows how quenching and termination alter the discretization-induced response at the fixed coarse step $h = 12$.

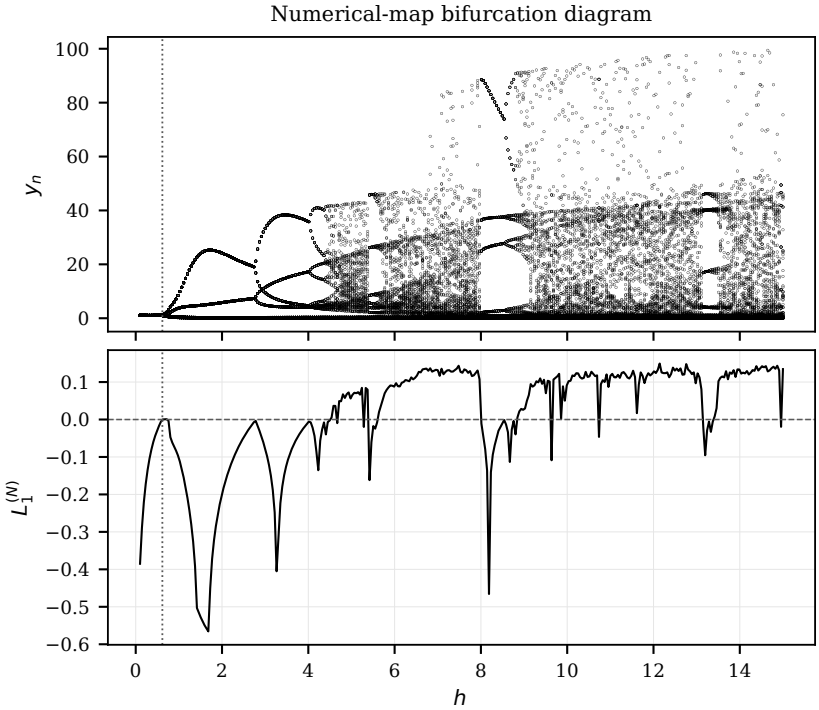

Figure 15. Step-size bifurcation diagram and largest finite-time Lyapunov exponent. The vertical line marks $h_c \approx 0.617496$, the first loss of equilibrium stability by the numerical discretization.

17 Initial-condition classification

Figure 18 classifies a 180×180 grid of initial conditions. After 5000 transients, 256 iterates are retained. Periods 1–64 are tested by requiring the maximum Euclidean mismatch over the last 96 paired states to be below 10^{-5}. At $h = 8.55$, subsets are classified as period 14, period 28 or another detected period. An unresolved point may represent a long transient or an aperiodic response and is not interpreted as a separate attractor.

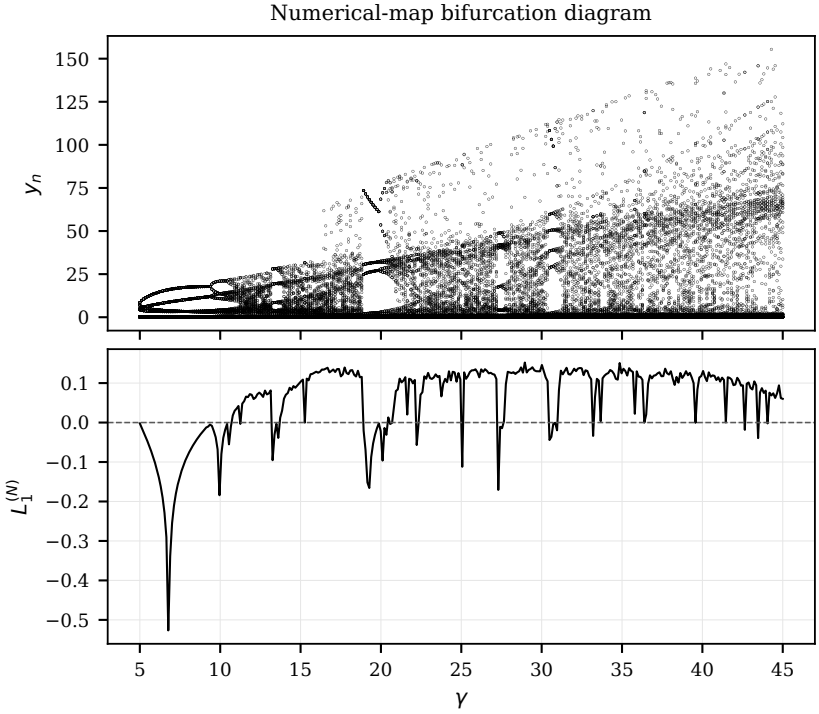

Figure 16. Discrete bifurcation diagram and largest finite-time Lyapunov exponent as γ varies at the coarse numerical step $h = 12$.

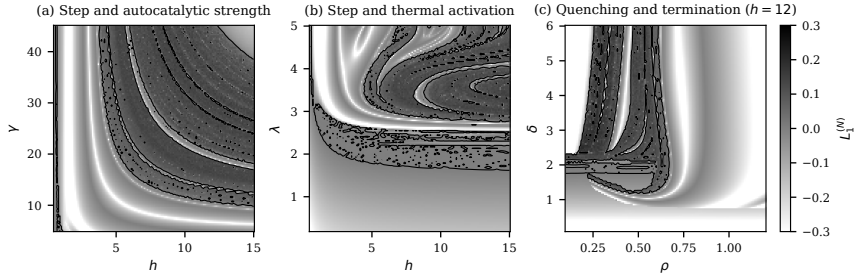

Figure 17. Finite-time Lyapunov diagrams. (a) (h, γ) plane. (b) (h, λ) plane. (c) (ρ, δ) plane at $h = 12$. Each panel uses a 140×140 grid, 1000 transient iterations and 1000 tangent updates. Black curves approximate $L_1^{(N)} = 0$.

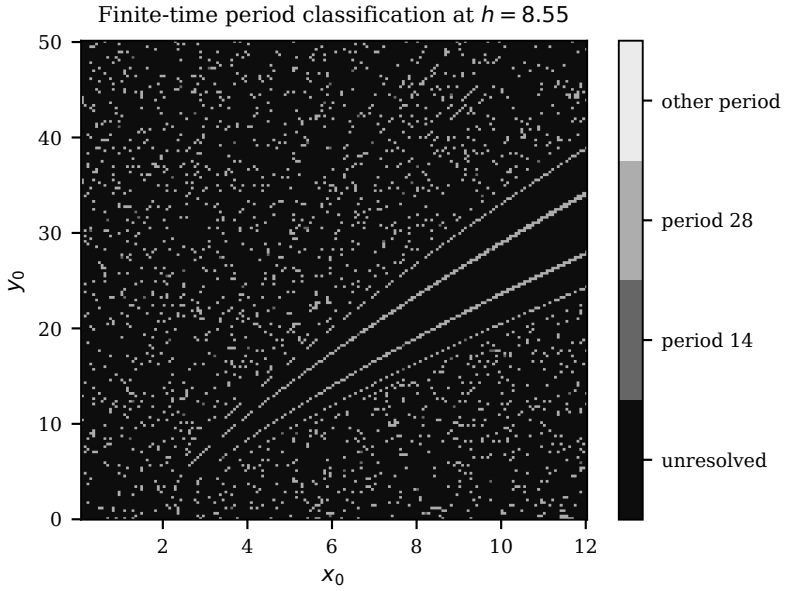

Figure 18. Finite-time period/convergence map over initial concentrations at $h = 8.55$. Categories identify period-14, period-28, other detected periods up to 64, and responses unresolved after the stated transient.

18 Chemical interpretation and scope

The continuous model is deliberately reduced, but its kinetic terms correspond to recognizable chemical roles. The source α represents slow activation of a precursor pool, and βx represents background formation of the autocatalyst. The saturated rate $\mathcal{R}(y)x$ approximates finite productivity of the $A + 2B \to 3B$ route when ideal cubic mass action is weakened by crowding, complexation, diffusion limitation, or competing inactive channels. Cross-quenching ρxy removes both active intermediates, while δy^2 represents bimolecular termination or dimerization.

The thermal multiplier is an empirical concentration-only closure. It is suitable for a qualitative two-variable study but does not establish thermodynamic consistency for a specified reagent system. A calibrated model should retain an energy equation, estimate activation and heat-transfer parameters, and compare simulated temperature and concentration histories

with experiment.

The reaction–diffusion extension is likewise conditional. The coefficients D_x and D_y are effective transport parameters, and the Turing calculation requires the precursor-like field to diffuse sufficiently faster than the autocatalyst-like field. This separation may be plausible if B is immobilized, reversibly bound, or transported through a more restrictive phase, but no such mechanism is identified or calibrated here. The computed patterns are therefore mechanistic possibilities under the stated diffusion assumptions.

The numerical step h is not a chemical rate constant. It characterizes the computational method used to approximate the kinetic equations. If a sampled, pulsed, or periodically diluted reactor is to be studied, its stroboscopic map should be derived explicitly as a composition of continuous flow and a physical reset or input operator. Such a map would generally differ from (77)–(78).

Table 7. Interpretation of the model and numerical quantities.

Quantity	Interpretation
α	effective precursor activation or feed strength
βx	non-catalysed production of B from A
$\mathcal{R}(y)x$	saturated, thermally enhanced autocatalytic conversion
ρxy	cross-quenching or inactive-adduct formation
δy^2	bimolecular termination or dimerization of B
D_x, D_y	effective diffusivities in the spatial extension
h	numerical time-step parameter of the semi-implicit discretization

19 Discussion

The continuous kinetics, reaction–diffusion system, and numerical map answer distinct stability questions. The well-mixed flow is positive and dissipative and supports Hopf-generated oscillations. Spatial coupling may destabilize a well-mixed stable equilibrium when the Neumann spectrum intersects the analytically determined band. The semi-implicit update preserves non-negative states and equilibria, but its local and global dynamics need not reproduce those of the flow.

For the reference set (42), both kinetic diagonal entries are negative, which excludes the two-component diffusion-driven mechanism considered here. Selected members of the Hopf parameter family instead have stable homogeneous kinetics and positive autocatalyst self-feedback. With sufficiently rapid precursor diffusion, they possess unstable nonconstant modes. The simulated spots, stripes, and square-symmetric structures are consistent with the predicted bands. The refinement evidence supports convergence of the P3 field, whereas P1 and P2 remain finite-time morphology demonstrations whose dominant wavelengths vary under refinement.

The fixed-point threshold h_c is not an accuracy threshold. The numerical map can incur large transient errors for $h < h_c$, and its first-order convergence becomes evident only when the step is small relative to the fastest local timescale $1/133.296 \approx 0.0075$. The period-10 orbit at $h = 4$ and the positive-exponent responses at larger steps are therefore examples of coarse-step dynamic inconsistency, not approximations of chaotic chemical dynamics. This interpretation agrees with elementary and topological dynamic-consistency theory [2, 3, 8, 29].

The contribution lies in the joint analysis of a bounded saturated rate law across three mathematical settings. For the continuous kinetics, positivity, dissipativity, equilibrium structure, and Hopf criticality are established or computed under stated hypotheses. For the spatial extension, the admissible Neumann modes are tested directly and the nonlinear patterns are reported with explicit convergence qualifications. For the numerical map, Schur stability, the full orbitwise Jacobian, Lyapunov diagnostics, and trajectory refinement are compared with the continuous flow. This

comparison distinguishes the study from analyses of Turing instability of periodic solutions, network-coupled patterns, and discrete-time chemical models considered independently of an underlying flow [6, 22, 38, 39]. The chemical interpretation nevertheless remains conditional because the thermal factor and diffusivities are phenomenological. Quantitative prediction requires an explicit energy balance, measured kinetic and transport parameters, and validation for a specified reaction.

20 Conclusion

A saturated two-intermediate autocatalytic model with phenomenological thermal activation has been analysed. The continuous flow preserves non-negative concentrations, possesses an absorbing region, and admits at least one positive equilibrium. The scalar equilibrium equation provides an a priori bound, a conditional uniqueness test, and the identity $\det J_c(E^*) = -\Psi'(y^*)$. The saddle-node and Hopf criteria include the hypotheses required by the corresponding local bifurcation theorems. For the illustrative parameter family, two transversal Hopf points have negative normalized first Lyapunov coefficients and generate locally attracting periodic orbits on the unstable-equilibrium side.

The reaction–diffusion extension is globally positive and bounded and provides an exact finite-domain instability test through the Neumann spectrum. Three well-mixed stable cases exhibit conditional diffusion-driven pattern formation; the numerical evidence is separated into a converged case and finite-time morphology examples. The semi-implicit discretization preserves positivity and equilibria but loses fixed-point stability at $h_c \approx 0.617496$ and can produce large transient errors even below this value. Its coarse-step periodic and positive-exponent responses are numerical-map dynamics.

Chemical positivity, homogeneous stability, spatial-mode stability, numerical fixed-point stability, and trajectory accuracy are therefore logically independent. Future work should replace the concentration-only thermal closure by a calibrated energy equation, determine transport parameters experimentally, and construct a dynamically consistent integrator for the stiff kinetics.

***Acknowledgment*:** This study is supported via funding from Prince Sattam bin Abdulaziz University, project number (PSAU/2026/R/1448). The authors extend their appreciation to the Deanship of Scientific Research at Northern Border University, Arar, KSA for funding this research through the project number "NBU-FFMRA-2026-2483-06".

References

[1] R. Anguelov, J. M. S. Lubuma, Contributions to the mathematics of the nonstandard finite difference method and applications, *Num. Methods Partial Diff. Eqs.* **17** (2001) 518–543, **doi:** 10.1002/num.1025.

[2] R. Anguelov, J. M. S. Lubuma, M. Shillor, Topological dynamic consistency of nonstandard finite difference schemes for dynamical systems, *J. Diff. Eq. Appl.* **17** (2011) 1769–1791, **doi:** 10.1080/10236198.2010.488226.

[3] M. Biswas, N. Bairagi, On the dynamic consistency of a two-species competitive discrete system with toxicity: local and global analysis, *J. Comput. Appl. Math.* **363** (2020) 145–155, **doi:** 10.1016/j.cam.2019.06.005.

[4] V. Castets, E. Dulos, J. Boissonade, P. De Kepper, Experimental evidence of a sustained standing Turing-type nonequilibrium chemical pattern, *Phys. Rev. Lett.* **64** (1990) 2953–2956, **doi:** 10.1103/PhysRevLett.64.2953.

[5] M. Chen, J. Kim, S. Ham, Patterns of a general chemical model involving the Degn–Harrison reaction scheme, *MATCH Commun. Math. Comput. Chem.* **93** (2025) 267–290, **doi:** 10.46793/match.93-2.267C.

[6] M. Chen, X. Li, X. Z. Li, R. Wu, Turing instability of equilibrium and periodic solution for an enzyme-catalyzed system, *MATCH Commun. Math. Comput. Chem.* **95** (2026) 659–694, **doi:** 10.46793/match.95-3.26625.

[7] M. Chen, X. Z. Li, Stability analysis and Turing pattern of an enzyme-catalyzed reaction model, *MATCH Commun. Math. Comput. Chem.* **94** (2025) 195–214, **doi:** 10.46793/match.94-1.195C.

[8] J. Cresson, F. Pierret, Nonstandard finite difference scheme preserving dynamical properties, *J. Comput. Appl. Math.* **303** (2016) 15–30, **doi:** 10.1016/j.cam.2016.02.007.

[9] D. T. Dimitrov, H. V. Kojouharov, Nonstandard finite-difference schemes for general two-dimensional autonomous dynamical systems, *Appl. Math. Lett.* **18** (2005) 769–774, **doi:** 10.1016/j.aml.2004.08.011.

[10] H. Dimsey, L. K. Forbes, A. P. Bassom, C. Quinn, A mathematical model of the Bray–Liebhafsky reaction, *Proc. R. Soc. A* **480** (2024) #20230964, **doi:** 10.1098/rspa.2023.0964.

[11] Q. Din, U. Saeed, Stability, discretization, and bifurcation analysis for a chemical reaction system, *MATCH Commun. Math. Comput. Chem.* **90** (2023) 151–174, **doi:** 10.46793/match.90-1.151D.

[12] Q. Din, M. S. Shabir, M. A. Khan, A cubic autocatalator chemical reaction model with limit cycle analysis and consistency-preserving discretization, *MATCH Commun. Math. Comput. Chem.* **87** (2022) 441–462, **doi:** 10.46793/match.87-2.441D.

[13] B. Dúzs, I. Lagzi, I. Szalai, Functional rhythmic chemical systems governed by pH-driven kinetic feedback, *ChemSystemsChem* **5** (2023) #e202200032, **doi:** 10.1002/syst.202200032.

[14] I. R. Epstein, J. A. Pojman, *An Introduction to Nonlinear Chemical Dynamics: Oscillations, Waves, Patterns, and Chaos*, Oxford Univ. Press, New York, 1998.

[15] R. J. Field, R. M. Noyes, Oscillations in chemical systems. IV. Limit cycle behavior in a model of a real chemical reaction, *J. Chem. Phys.* **60** (1974) 1877–1884, **doi:** 10.1063/1.1681288.

[16] X. Gao, Y. Jin, M. Marwan, F. Li, Y. Wei, Impact of Hopf and Bautin bifurcations on an autocatalytic chemical reaction system, *MATCH Commun. Math. Comput. Chem.* **94** (2025) 863–889, **doi:** 10.46793/match.94-3.09225.

[17] P. Gray, S. K. Scott, Autocatalytic reactions in the isothermal, continuous stirred tank reactor: isolas and other forms of multistability, *Chem. Eng. Sci.* **38** (1983) 29–43, **doi:** 10.1016/0009-2509(83)80132-8.

[18] P. Gray, S. K. Scott, Autocatalytic reactions in the isothermal, continuous stirred tank reactor: oscillations and instabilities in the system $A + 2B \to 3B$, $B \to C$, *Chem. Eng. Sci.* **39** (1984) 1087–1097, **doi:** 10.1016/0009-2509(84)87017-7.

[19] J. Guckenheimer, P. Holmes, *Nonlinear Oscillations, Dynamical Systems, and Bifurcations of Vector Fields*, Springer, New York, 1983.

[20] D. Henry, *Geometric Theory of Semilinear Parabolic Equations*, Springer, Berlin, 1981, **doi:** 10.1007/BFb0089647.

[21] M. Izadi, H. Ahmad, H. M. Srivastava, Numerical computations of time-dependent auto-catalytic glycolysis chemical reaction–diffusion system, *MATCH Commun. Math. Comput. Chem.* **93** (2025) 69–97, **doi:** 10.46793/match.93-1.069I.

[22] M. S. Khan, M. A. Khan, Q. Din, W. Abdelfattah, Two-parameter bifurcation analysis of a discrete-time glycolysis model, *MATCH Commun. Math. Comput. Chem.* **94** (2025) 581–603, **doi:** 10.46793/match94-3.29224.

[23] Y. A. Kuznetsov, *Elements of Applied Bifurcation Theory*, Springer, New York, 2004.

[24] E. Lantos, G. Mótyán, E. Frank, R. Eelkema, J. van Esch, D. Horváth, A. Tóth, Dynamics of hydroxide-ion-driven reversible autocatalytic networks, *RSC Adv.* **13** (2023) 20243–20247, **doi:** 10.1039/D3RA04215D.

[25] J. H. Merkin, D. J. Needham, S. K. Scott, Oscillatory chemical reactions in closed vessels, *Proc. R. Soc. Lond. A* **406** (1986) 299–323, **doi:** 10.1098/rspa.1986.0077.

[26] R. E. Mickens, Nonstandard finite difference schemes for differential equations, *J. Diff. Eq. Appl.* **8** (2002) 823–847, **doi:** 10.1080/1023619021000000807.

[27] R. E. Mickens, Calculation of denominator functions for nonstandard finite difference schemes for differential equations satisfying a positivity condition, *Num. Methods Partial Diff. Eqs.* **23** (2007) 672–691, **doi:** 10.1002/num.20198.

[28] G. Nicolis, I. Prigogine, *Self-Organization in Nonequilibrium Systems*, Wiley, New York, 1977.

[29] S. Ohmori, Y. Yamazaki, Types and stability of fixed points for positivity-preserving discretized dynamical systems in two dimensions, *JSIAM Lett.* **15** (2023) 73–76, **doi:** 10.14495/jsiaml.15.73.

[30] Q. Ouyang, H. L. Swinney, Transition from a uniform state to hexagonal and striped Turing patterns, *Nature* **352** (1991) 610–612, **doi:** 10.1038/352610a0.

[31] M. Pezzella, High order positivity-preserving numerical methods for a non-local photochemical model, *ESAIM Math. Model. Num. Anal.* **59** (2025) 1763–1790, **doi:** 10.1051/m2an/2025041.

[32] S. Salzman, L. K. Forbes, C. R. Quinn, Oscillations and tipping points in a model thermokinetic reaction, *Proc. Royal Soc. A* **480** (2024) #20240304, **doi:** 10.1098/rspa.2024.0304.

[33] S. K. Scott, *Chemical Chaos*, Clarendon Press, Oxford, 1991.

[34] E. E. Sel'kov, Self-oscillations in glycolysis. 1. A simple kinetic model, *Eur. J. Biochem.* **4** (1968) 79–86, **doi:** 10.1111/j.1432-1033.1968.tb00175.x.

[35] S. H. Strogatz, *Nonlinear Dynamics and Chaos: With Applications to Physics, Biology, Chemistry, and Engineering*, Westview Press, Boulder, 2015.

[36] A. M. Turing, The chemical basis of morphogenesis, *Phil. Trans. Royal Soc. London B* **237** (1952) 37–72, **doi:** 10.1098/rstb.1952.0012.

[37] J. J. Tyson, *The Belousov–Zhabotinsky Reaction*, Springer, Berlin, 1976.

[38] X. Zhao, X. Z. Li, M. Chen, Spatiotemporal oscillations of an enzyme-catalyzed model, *MATCH Commun. Math. Comput. Chem.* **94** (2025) 605–631, **doi:** 10.46793/match94-3.04925.

[39] J. Zhou, X. Hua, Y. Chen, Y. Ye, Pattern formation in an enzyme-catalyzed reaction–diffusion system on complex networks: the coupling mechanism of topology and dynamics, *MATCH Commun. Math. Comput. Chem.* **96** (2026) 99–128, **doi:** 10.46793/match.96-1.29925.